

Interaction between solitary waves and a combined structure of two concentric asymmetric porous arc walls

Cite as: Phys. Fluids **34**, 042103 (2022); <https://doi.org/10.1063/5.0087878>

Submitted: 10 February 2022 • Accepted: 15 March 2022 • Published Online: 01 April 2022

Zhenfeng Zhai (翟振峰),  Siming Zheng (郑思明) and  Decheng Wan (万德成)



[View Online](#)



[Export Citation](#)



[CrossMark](#)

APL Machine Learning

Open, quality research for the networking communities

OPEN FOR SUBMISSIONS **MAY 2022**

[LEARN MORE](#)





Interaction between solitary waves and a combined structure of two concentric asymmetric porous arc walls

Cite as: Phys. Fluids **34**, 042103 (2022); doi: [10.1063/5.0087878](https://doi.org/10.1063/5.0087878)

Submitted: 10 February 2022 · Accepted: 15 March 2022 ·

Published Online: 1 April 2022



Zhenfeng Zhai (翟振峰),¹ Siming Zheng (郑思明),^{2,3}  and Decheng Wan (万德成)^{4,a)} 

AFFILIATIONS

¹School of Ocean Engineering and Technology, Sun Yat-Sen University, Zhuhai 519000, China

²School of Engineering, Computing, and Mathematics, University of Plymouth, Drake Circus, Plymouth PL48AA, United Kingdom

³State Key Laboratory of Hydrosience and Engineering, Tsinghua University, Beijing 100084, China

⁴Computational Marine Hydrodynamics Lab (CMHL), School of Naval Architecture, Ocean, and Civil Engineering, Shanghai Jiao Tong University, Shanghai 200240, China

^{a)} Author to whom correspondence should be addressed: dcwan@sjtu.edu.cn

ABSTRACT

An analytical model based on the linear potential flow theory is developed to study the diffraction problem of solitary wave interaction with a combined structure of two thin concentric asymmetric porous arc walls. The two closed virtual circles, where the two arc walls are located, are used to partition the entire fluid region into three sub-regions; the velocity potentials associated with each region are expanded in terms of a series of appropriate eigenfunctions. Furthermore, a series of simultaneous equations are used to determine the unknown coefficients in the expressions of the velocity potentials. The accuracy of the present model is verified by comparing its output with published results. Meanwhile, the impact of various important parameters (i.e., annular spacing, incident angle, the orientation of two arc walls, and porosity of walls) with respect to wave forces and relative wave height is examined. Numerical results reveal that dual-arc walls provide more significant protection for the interior cylinder than single walls. The two cross-placed arc walls provide excellent protection for the interior cylinder with their sheltered area extended. This research is anticipated to provide useful theoretical guidance for nearshore engineering design.

Published under an exclusive license by AIP Publishing. <https://doi.org/10.1063/5.0087878>

I. INTRODUCTION

Porous structures are widely used in marine engineering, because they dissipate wave energy by allowing partial waves to pass through, therefore protecting coastal and marine structures from direct wave impact. Different types of porous structures are used in constructing bridges, breakwaters, docks, etc. Among them, porous cylindrical structures are very suitable for the construction of coastal and marine structures. Accordingly, researchers in fluids physics and coastal/ocean engineering have focused on wave motion by considering porous cylindrical structures.

When water waves impinge on impermeable structures, strong wave reflections and large wave loads appear on the structure surface, posing a risk to the structures. To reduce the potential risks, many theoretical, numerical, and experimental studies regarding the diffraction of water waves by porous cylindrical structures have been investigated over the years. Several scholars have conducted studies on the interaction between different kinds of waves such as short-crested waves

(Song and Tao, 2007; Tao and Chakrabarti, 2009; Liu and Lin, 2013), Airy waves (Wang and Ren, 1994; Darwiche *et al.*, 1994; Vijayalakshmi *et al.*, 2008), cnoidal waves (Weng *et al.*, 2016; Zhai *et al.*, 2021b), solitary waves (Zhong and Wang, 2006; Sankarbabu *et al.*, 2008; Miao and Wang, 2021), and a concentric cylindrical system. Through their research, in-depth understanding of the key characteristics of concentric structures has been gained. These characteristics, which include the coefficient of permeable walls and the ratio of inner to outer radii, are the key factors affecting the protective effect of the outer permeable wall on the inner cylinder. Additionally, water wave interaction with compound cylinders has also drawn some researchers' attention. Sarkar and Bora (2020) investigated diffraction of Airy waves by a specific type of cylinders, i.e., a floating surface-piercing truncated partial-porous cylinder and then a surface-piercing bottom-mounted truncated partial-porous cylinder, by treating both cases separately. More recently, Sarkar and Bora (2021) examined the case of a train of linear water waves incident on a

bottom-mounted surface-piercing compound partial-porous cylinder. The cylinder consisted of two coaxial cylinders: the upper and lower cylinders. The upper cylinder was hollow with a thin porous sidewall, and the lower cylinder (with a radius greater than that of the upper cylinder) was rigid. To cope with the more complex marine environment and better protect the internal structure, Liu *et al.* (2018b) employed a semi-analytical solution method to solve the problem of water wave interaction with a concentric structure having multiple permeable outer walls. They found that by adjusting proportions of the parameters and radius ratios of the protective walls, more protective walls can better balance the wave elevations and excitation forces among them. Liu *et al.* (2018a) examined the diffraction of Airy waves caused by combined cylindrical and perforated structures with arbitrary smooth cross-sections in both theory and experiment. Steiros *et al.* (2020) analyzed the drag of various types of porous cylinders, bars, and plates under steady laminar inflow. They found that the drag decreases with increased porosity in most cases, while some special types of perforations can increase the drag on both cylinders and bars, either by enhancing the effect of the rear half of the models or by organizing the wake structures. Zheng *et al.* (2020b) investigated wave diffraction from an array of structured cylinders, which are composed of a number of thin plates deployed in parallel in the water of finite depth based on a linear potential flow theory and an eigenfunction expansion method. Under the assumption of small-amplitude water wave motion and structural response, Zheng *et al.* (2020a) investigated the hydroelastic interaction between water waves and multiple submerged porous elastic disks with negligible thickness in water of a finite depth. Zamponi *et al.* (2021) calculated the distortion of homogeneous isotropic turbulence interacting with a porous cylinder by means of the rapid distortion theory. They investigated the impact of porosity on the velocity field through the analysis of the one-dimensional spectra at different locations near the porous cylinder and the velocity variance along the stagnation streamline. Li and Liu (2021) studied water wave scattering by a submerged horizontal bottom-mounted semi-circular barrier in a two-layer fluid based on the linear potential flow theory. Liang *et al.* (2021) investigated the scattering of water waves by impermeable and perforated horizontal plates considering both circular and elliptical plates within the framework of the linear potential flow theory. Ma *et al.* (2022) proposed a new semi-analytical solution to study the interactions between water waves and a thin porous shell net cage that is submerged at different depths below the mean water level.

In deep and distant ocean locations, circular breakwaters are generally employed to protect the interior of the main structure while confronting the incoming waves in all directions. Despite the circular wall's excellent performance, its use as nearshore protection is excessive and expensive. For these reasons, designers and engineers have designed and built a number of unenclosed marine nearshore structures, such as arc-shaped and V-shaped breakwaters, to minimize the construction cost and maintain adequate protection. One example of these applications in offshore engineering is the arc-shaped breakwater, which has been successfully applied in the Caspian Sea (see Fig. 1). Cheng *et al.* (2007) analyzed the wave surface variation in the permeable arc-shaped breakwater with a range of wave and breakwater parameters. Chang *et al.* (2012) analyzed the water wave diffraction caused by a V-type wall. Lin and Liu (2012) conducted a numerical investigation of the interaction between a short-crested wave and a concentric system with two arc walls. Christensen *et al.* (2018) studied



FIG. 1. Multiple arc-shaped breakwaters applied in the Kashagan Oilfield in Caspian Sea, Kazakhstan.

the effect of two different damping mechanisms of a floating breakwater through model test and numerical simulation. Han *et al.* (2021) used a three-dimensional computational fluid dynamics model to simulate the oblique wave diffraction around an arc breakwater. They experimentally measured the pressure distribution and wave forces at different downstream sections of different waves to verify the accuracy of their numerical calculations. Zhai *et al.* (2021a) compared the hydrodynamic performance V-shaped and arc-shaped breakwater. Most of the previous studies have been implemented with the assumption of the action of waves with a small amplitude. However, the utilization of shallow water wave theories, such as the solitary wave theory, for structures in shallow water areas is more appropriate. The studies on the interaction of solitary waves with arc-type structures are limited. To the best of the authors' knowledge, the interaction between solitary waves and asymmetric porous arc walls has never been studied.

The primary objective of this work is to theoretically investigate the diffraction problem of solitary wave interaction with a combined structure having two concentric asymmetric porous arc walls. By comparing the results of the current model with those of existing research, its accuracy is confirmed. The total non-dimensional hydrodynamic forces, wave run-ups on the solid cylinder, and relative wave heights in the vicinity of the present structure are analyzed. This paper is laid out as follows: The problem is formulated in Sec. II. The validity of the proposed model is examined in Sec. III. Then, the analytical results are presented in Sec. IV before the work is summarized in Sec. V.

II. THEORETICAL FORMULATION

A. Governing equations and boundary conditions

A schematic of a solitary wave interacting with an impermeable cylinder and two concentric asymmetric arcs having negligible thickness is shown in Fig. 2. The still water depth is h ; the radii of arc walls 1 and 2 and the impermeable cylinder are denoted as a , b , and c , respectively. A cylindrical coordinate system (O, r, θ, z) is employed with the z -axis pointing upward from the flat water bottom. The central angles of arc walls 1 and 2 are indicated as γ_1 and γ_2 , respectively; moreover, the angle from the positive direction of the x -axis to one end of each arc wall is represented by α_1 and α_2 , respectively. Therefore, the position of arc walls in the coordinate system can be consistently determined by means of γ and α . Furthermore, the entire fluid region may be divided into three regions: outside region

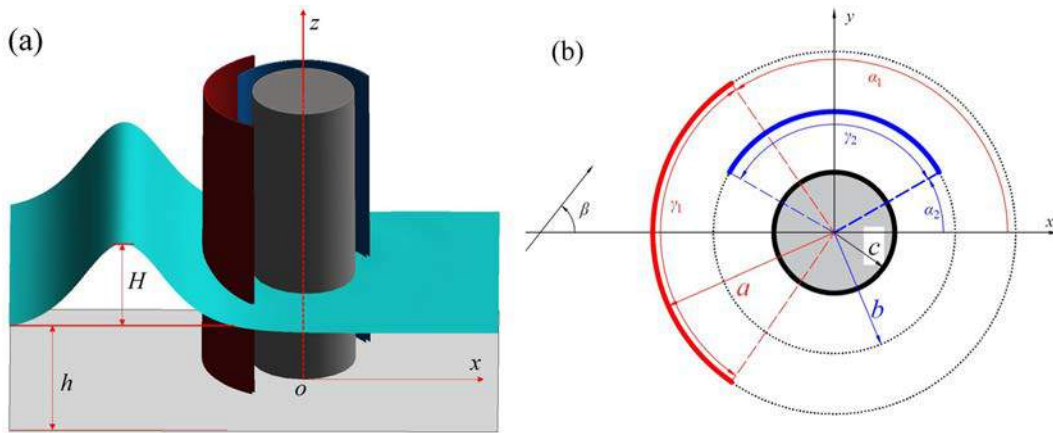


FIG. 2. Definition sketch: (a) bird's-eye ($\beta = 0$) and (b) plan view.

$\Omega_1 (r \geq a)$, annular region between the two arc walls $\Omega_2 (b \leq r \leq a)$, and inside region $\Omega_3 (c \leq r \leq b)$.

Assuming the fluid is inviscid, incompressible, and the motion irrotational. The velocity potential is given by $\Phi(r, \theta, z, t) = \text{Re} [\phi(r, \theta, z, t)]$, where ϕ is the complex velocity potential and t denotes the time. The velocity potential in the three regions can also be expressed as $\phi^{(j)} = \phi_I + \phi_s^{(j)} (j = 1, 2, 3)$, where ϕ_I and $\phi_s^{(j)}$ denote the incident and scattered potentials, respectively.

For the combined system subjected to solitary waves of height H and speed c_0 propagating along the positive direction of the x -axis, the free-surface elevation η_I can be written in the following form according to Isaacson (1983):

$$\eta_I = H \text{sech}^2 \left[\sqrt{\frac{3H}{4h^3}} (x - c_0 t) \right], \tag{1}$$

where $c_0 = \sqrt{gh}$ and g denote wave speed and acceleration due to gravity, respectively. Moreover, η_I may be represented as a Fourier integral

$$\eta_I = \frac{H}{2\pi} \int_{-\infty}^{\infty} A(k) e^{ik(x-c_0t)} dk, \tag{2}$$

in which $i = \sqrt{-1}$. The Fourier transform $A(k) = A(-k)$ of η_I is as follows:

$$A(k) = \frac{4\pi h^3 k}{3H} \text{cosech} \left[\pi k \sqrt{\frac{h^3}{3H}} \right]. \tag{3}$$

Then, the corresponding incident potential ϕ_I can be expressed as follows:

$$\phi_I = \frac{H}{2\pi\sqrt{h/g}} \int_{-\infty}^{\infty} \frac{A(k)}{ik} e^{ik(x-c_0t)} dk = \frac{H}{\pi\sqrt{h/g}} \int_0^{\infty} \frac{A(k)}{ik} e^{ikx} e^{-ikc_0t} dk. \tag{4}$$

Furthermore, ϕ_I can be rewritten as follows:

$$\phi_I = \int_0^{\infty} \hat{\phi}_I [k(x - c_0 t)] dk. \tag{5}$$

Evidently, $\hat{\phi}_I [k(x - c_0 t)]$ satisfies the relationship: $\frac{\partial \hat{\phi}_I}{\partial x} - ik \hat{\phi}_I = 0$. Meanwhile, the complex scattered potential is also rewritten as $\phi_s^{(1)} = \int_0^{\infty} \hat{\phi}_s^{(1)} dk$. Clearly, $\hat{\phi}_s^{(1)}$ must satisfy the following radiation condition, i.e.:

$$\lim_{r \rightarrow \infty} \sqrt{r} \left[\frac{\partial \hat{\phi}_s^{(1)}}{\partial r} - ik \hat{\phi}_s^{(1)} \right] = 0. \tag{6}$$

Furthermore, Eq. (4) can be expanded into a Fourier complex form using the following identity:

$$e^{ikx} = e^{ikr \cos \theta} = \sum_{n=-\infty}^{\infty} i^n J_n(kr) e^{in\theta} = \sum_{n=0}^{\infty} \zeta_n J_n(kr) \cos(n\theta), \tag{7}$$

in which $\zeta_0 = 1$, and $\zeta_n = 2i^n$ for $n \geq 1$; $J_n(\cdot)$ denotes the Bessel function of the first kind of order n .

For a solitary wave propagating at an angle β , the incident potential can be written as follows:

$$\phi_I = \frac{H}{\pi\sqrt{h/g}} \int_0^{\infty} \frac{A(k)}{ik} e^{-ikc_0t} \sum_{n=0}^{\infty} \zeta_n J_n(kr) \cos n(\theta - \beta) dk. \tag{8}$$

According to the matching principle, the continuity conditions of pressure and velocity must be satisfied on the arc walls and the virtual dividing surfaces, i.e.,

$$\phi^{(1)} = \phi^{(2)} \text{ for } r = a, \alpha_1 + \gamma_1 - 2\pi \leq \theta \leq \alpha_1, \tag{9}$$

$$\frac{\partial \phi^{(1)}}{\partial r} = \frac{\partial \phi^{(2)}}{\partial r} \text{ for } r = a, 0 \leq \theta \leq 2\pi, \tag{10}$$

$$\phi^{(2)} = \phi^{(3)} \text{ for } r = b, \alpha_2 + \gamma_2 - 2\pi \leq \theta \leq \alpha_2, \tag{11}$$

$$\frac{\partial \phi^{(2)}}{\partial r} = \frac{\partial \phi^{(3)}}{\partial r} \text{ for } r = b, 0 \leq \theta \leq 2\pi. \tag{12}$$

In addition, the boundary conditions on the porous walls are given by (Williams *et al.*, 2000)

$$\frac{\partial \phi^{(1)}}{\partial r} = \frac{\partial \phi^{(2)}}{\partial r} = \frac{G_1}{c_0} \left(\frac{\partial \phi^{(1)}}{\partial t} - \frac{\partial \phi^{(2)}}{\partial t} \right) \text{ for } r = a, \alpha_1 \leq \theta \leq \alpha_1 + \gamma_1, \tag{13}$$

$$\frac{\partial \phi^{(2)}}{\partial r} = \frac{\partial \phi^{(3)}}{\partial r} = \frac{G_2}{c_0} \left(\frac{\partial \phi^{(2)}}{\partial t} - \frac{\partial \phi^{(3)}}{\partial t} \right) \text{ for } r = b, \alpha_2 \leq \theta \leq \alpha_2 + \gamma_2, \tag{14}$$

where $G_j (j = 1, 2)$ denote porous-effect parameter as used by Chwang (1983), and it depends on the density of the holes deployed on the wall and the size of each hole. Furthermore, G can be expressed in the form $G_r + iG_i$ as used by Yu (1995), where G_r and G_i denote the real part and the imaginary part, respectively. Physically, G_r and G_i represent the drag term and the inertia term, which lead to the wave energy loss and the phase change, respectively. The porous-effect parameter can be expressed as $G = \rho c_0 L / \mu$, where ρ , c_0 , μ , and L are fluid density, wave speed, coefficient of dynamic viscosity, and material constants, which have the dimension of length, respectively. In particular, two limiting cases for the porous-effect parameter must be noted: (1) $G_j = 0$ indicates that the arc walls are completely dense; (2) $G_j \rightarrow +\infty$ means that completely translucent (i.e., they can be assumed to be inexistent).

B. Analytical solution

In region Ω_1 , $\phi^{(1)}$ is composed of the incident potential ϕ_I and scatter potential $\phi_s^{(1)}$, where $\phi_s^{(1)}$ must satisfy the radiation and boundary conditions in Eqs. (6), (9), (10), and (13), respectively. It may be written in the following form:

$$\phi_s^{(1)} = \frac{H}{\sqrt{h/g} \pi} \frac{1}{\pi} \int_0^\infty \frac{A(k)}{ik} e^{-ikc_0 t} \sum_{n=0}^\infty \left[A_n^{(1)} \cos(n\theta) H_n(kr) + B_n^{(1)} \sin(n\theta) H_n(kr) \right] dk, \tag{15}$$

where $A_n^{(1)}$ and $B_n^{(1)}$ are the potential coefficients to be determined and $H_n(\cdot)$ denotes the first kind Hankel function of the n th order. Thus, by combining Eqs. (8) and (15), $\phi^{(1)}$ can be expressed as follows:

$$\begin{aligned} \phi^{(1)} = \phi_I + \phi_s^{(1)} = & \frac{H}{\sqrt{h/g} \pi} \frac{1}{\pi} \int_0^\infty \frac{A(k)}{ik} e^{-ikc_0 t} \sum_{n=0}^\infty \left\{ [\xi_n J_n(kr) \cos(n\beta) \right. \\ & \left. + A_n^{(1)} H_n(kr)] \cos(n\theta) + [\xi_n J_n(kr) \sin(n\beta) \right. \\ & \left. + B_n^{(1)} H_n(kr)] \sin(n\theta) \right\} dk. \end{aligned} \tag{16}$$

In the two regions Ω_2 and Ω_3 , the diffracted potentials can be expressed as follows:

$$\begin{aligned} \phi^{(2)} = & \frac{H}{\sqrt{h/g} \pi} \frac{1}{\pi} \int_0^\infty \frac{A(k)}{ik} e^{-ikc_0 t} \sum_{n=0}^\infty \left\{ [A_n^{(2)} J_n(kr) + C_n H_n(kr)] \cos(n\theta) \right. \\ & \left. + [B_n^{(2)} J_n(kr) + D_n H_n(kr)] \sin(n\theta) \right\} dk, \end{aligned} \tag{17}$$

$$\begin{aligned} \phi^{(3)} = & \frac{H}{\sqrt{h/g} \pi} \frac{1}{\pi} \int_0^\infty \frac{A(k)}{ik} e^{-ikc_0 t} \sum_{n=0}^\infty \left[A_n^{(3)} \cos(n\theta) + B_n^{(3)} \sin(n\theta) \right] \\ & \times E_n(kr) dk, \end{aligned} \tag{18}$$

in which

$$E_n(kr) = \begin{cases} J_n(kr) - \frac{J'_n(kc)}{H'_n(kc)} H_n(kr) & \text{for } c \neq 0, \\ J_n(kr) & \text{for } c = 0, \end{cases} \tag{19}$$

in which $A_n^{(2)}$, $B_n^{(2)}$, $A_n^{(3)}$, $B_n^{(3)}$, C_n and D_n are the unknown potential coefficients to be determined.

By substituting the expressions of the velocity potentials in each region, i.e., Eqs. (16)–(18), into the boundary conditions as given in Eqs. (10) and (12), and applying the orthogonality properties of $\cos(m\theta)$ and $\sin(m\theta)$ over $[0, 2\pi]$, the following is derived:

$$\begin{cases} \xi_m \cos(m\beta) J'_m(ka) + A_m^{(1)} H'_m(ka) \\ = A_m^{(2)} J'_m(ka) + C_m H'_m(ka), & m = 0, 1, \dots, \\ \xi_m \sin(m\beta) J'_m(ka) + B_m^{(1)} H'_m(ka) \\ = B_m^{(2)} J'_m(ka) + D_m H'_m(ka), & m = 1, 2, \dots, \\ A_m^{(2)} J'_m(kb) + C_m H'_m(kb) = A_m^{(3)} E'_m(kb), & m = 0, 1, \dots, \\ B_m^{(2)} J'_m(kb) + D_m H'_m(kb) = B_m^{(3)} E'_m(kb), & m = 1, 2, \dots \end{cases} \tag{20}$$

Next, substituting the velocity potentials in each region in Eqs. (16)–(18) into other boundary conditions in Eqs. (9), (11), (13), and (14) yields the following:

$$\begin{aligned} p_1(\theta) = & \sum_{n=0}^\infty \left\{ [\xi_n \cos(n\beta) J_n(ka) + A_n^{(1)} H_n(ka)] \cos(n\theta) \right. \\ & \left. + [\xi_n \sin(n\beta) J_n(ka) + B_n^{(1)} H_n(ka)] \sin(n\theta) \right. \\ & \left. - [A_n^{(2)} J_n(ka) + C_n H_n(ka)] \cos(n\theta) \right. \\ & \left. - [B_n^{(2)} J_n(ka) + D_n H_n(ka)] \sin(n\theta) \right\} \\ = & 0, \alpha_1 + \gamma_1 - 2\pi \leq \theta \leq \alpha_1, \end{aligned} \tag{21a}$$

$$\begin{aligned} p_2(\theta) = & \sum_{n=0}^\infty \left\{ \xi_n iG_1 J_n(ka) \cos(n\beta) \cos(n\theta) + A_n^{(1)} iG_1 H_n(ka) \cos(n\theta) \right. \\ & \left. + A_n^{(2)} [J'_n(ka) - iG_1 J_n(ka)] \cos(n\theta) + C_n [H'_n(ka) \right. \\ & \left. - iG_1 H_n(ka)] \cos(n\theta) + \xi_n iG_1 J_n(ka) \sin(n\beta) \sin(n\theta) \right. \\ & \left. + B_n^{(1)} iG_1 H_n(ka) \sin(n\theta) + B_n^{(2)} [J'_n(ka) - iG_1 J_n(ka)] \right. \\ & \left. \times \sin(n\theta) + D_n [H'_n(ka) - iG_1 H_n(ka)] \sin(n\theta) \right\} \\ = & 0, \alpha_1 \leq \theta \leq \alpha_1 + \gamma_1, \end{aligned} \tag{21b}$$

$$\begin{aligned} q_1(\theta) = & \sum_{n=0}^\infty \left\{ [A_n^{(2)} J_n(kb) + C_n H_n(kb) - A_n^{(3)} E_n(kb)] \cos(n\theta) \right. \\ & \left. + [B_n^{(2)} J_n(kb) + D_n H_n(kb) - B_n^{(3)} E_n(kb)] \sin(n\theta) \right\} \\ = & 0, \alpha_2 + \gamma_2 - 2\pi \leq \theta \leq \alpha_2, \end{aligned} \tag{21c}$$

$$q_2(\theta) = \sum_{n=0}^{\infty} \{A_n^{(3)} [E'_n(kb) - iG_2 E_n(kb)] \cos(n\theta) + A_n^{(2)} iG_2 J_n(kb) \cos(n\theta) + C_n iG_2 H_n(kb) \cos(n\theta) + B_n^{(3)} [E'_n(kb) - iG_2 E_n(kb)] \sin(n\theta) + B_n^{(2)} iG_2 J_n(kb) \sin(n\theta) + D_n iG_2 H_n(kb) \sin(n\theta)\} = 0, \alpha_2 \leq \theta \leq \alpha_2 + \gamma_2, \tag{21d}$$

where the custom functions $p_j(\theta)$ and $q_j(\theta)$ ($j = 1, 2$) can be combined into two piecewise functions $P(\theta)$ and $Q(\theta)$, respectively, as follows:

$$P(\theta) = \begin{cases} p_1(\theta) & (\alpha_1 + \gamma_1 - 2\pi \leq \theta \leq \alpha_1) \\ p_2(\theta) & (\alpha_1 \leq \theta \leq \alpha_1 + \gamma_1) \end{cases} = 0, \tag{22}$$

$$Q(\theta) = \begin{cases} q_1(\theta) & (\alpha_2 + \gamma_2 - 2\pi \leq \theta \leq \alpha_2) \\ q_2(\theta) & (\alpha_2 \leq \theta \leq \alpha_2 + \gamma_2) \end{cases} = 0, \tag{23}$$

$$\begin{cases} \int_0^{2\pi} \cos(m\theta) P(\theta) d\theta = 0, & m = 0, 1, \dots, \\ \int_0^{2\pi} \sin(m\theta) P(\theta) d\theta = 0, & m = 1, 2, \dots, \\ \int_0^{2\pi} \cos(m\theta) Q(\theta) d\theta = 0, & m = 0, 1, \dots, \\ \int_0^{2\pi} \sin(m\theta) Q(\theta) d\theta = 0, & m = 1, 2, \dots \end{cases} \tag{24}$$

The substitution of the self-defining functions $p_j(\theta)$ and $q_j(\theta)$ ($j = 1, 2$) into Eq. (24) yields the following:

$$\begin{aligned} & \sum_{n=0}^{\infty} \{ \xi_n J_n(ka) \cos(n\beta) [T_{nm}^{11} + iG_1 T_{nm}^{13}] + \zeta_n J_n(ka) \sin(n\beta) [T_{nm}^{12} + iG_1 T_{nm}^{14}] \} + \sum_{n=0}^{\infty} A_n^{(1)} H_n(ka) [T_{nm}^{11} + iG_1 T_{nm}^{13}] \\ & + \sum_{n=1}^{\infty} B_n^{(1)} H_n(ka) [T_{nm}^{12} + iG_1 T_{nm}^{14}] + \sum_{n=0}^{\infty} A_n^{(2)} [J'_n(ka) T_{nm}^{13} - iG_1 J_n(ka) T_{nm}^{13} - J_n(ka) T_{nm}^{11}] \\ & + \sum_{n=1}^{\infty} B_n^{(2)} [J'_n(ka) T_{nm}^{14} - iG_1 J_n(ka) T_{nm}^{14} - J_n(ka) T_{nm}^{12}] + \sum_{n=0}^{\infty} C_n [H'_n(ka) T_{nm}^{13} - iG_1 H_n(ka) T_{nm}^{13} - H_n(ka) T_{nm}^{11}] \\ & + \sum_{n=1}^{\infty} D_n [H'_n(ka) T_{nm}^{14} - iG_1 H_n(ka) T_{nm}^{14} - H_n(ka) T_{nm}^{12}] = 0, \quad m = 0, 1, 2, \dots, \end{aligned} \tag{25a}$$

$$\begin{aligned} & \sum_{n=0}^{\infty} \{ \xi_n J_n(ka) \cos(n\beta) [T_{nm}^{15} + iG_1 T_{nm}^{17}] + \zeta_n J_n(ka) \sin(n\beta) [T_{nm}^{16} + iG_1 T_{nm}^{18}] \} + \sum_{n=0}^{\infty} A_n^{(1)} H_n(ka) [T_{nm}^{15} + iG_1 T_{nm}^{17}] \\ & + \sum_{n=1}^{\infty} B_n^{(1)} H_n(ka) [T_{nm}^{16} + iG_1 T_{nm}^{18}] + \sum_{n=0}^{\infty} A_n^{(2)} [J'_n(ka) T_{nm}^{17} - iG_1 J_n(ka) T_{nm}^{17} - J_n(ka) T_{nm}^{15}] \\ & + \sum_{n=1}^{\infty} B_n^{(2)} [J'_n(ka) T_{nm}^{18} - iG_1 J_n(ka) T_{nm}^{18} - J_n(ka) T_{nm}^{16}] + \sum_{n=0}^{\infty} C_n [H'_n(ka) T_{nm}^{17} - iG_1 H_n(ka) T_{nm}^{17} - H_n(ka) T_{nm}^{15}] \\ & + \sum_{n=1}^{\infty} D_n [H'_n(ka) T_{nm}^{18} - iG_1 H_n(ka) T_{nm}^{18} - H_n(ka) T_{nm}^{16}] = 0, \quad m = 1, 2, 3, \dots, \end{aligned} \tag{25b}$$

$$\begin{aligned} & \sum_{n=0}^{\infty} A_n^{(2)} J_n(kb) [T_{nm}^{21} + iG_2 T_{nm}^{23}] + \sum_{n=0}^{\infty} A_n^{(3)} [E'_n(kb) T_{nm}^{23} - iG_2 E_n(kb) T_{nm}^{23} - E_n(kb) T_{nm}^{21}] + \sum_{n=1}^{\infty} B_n^{(2)} J_n(kb) [T_{nm}^{22} + iG_1 T_{nm}^{24}] + \sum_{n=1}^{\infty} B_n^{(3)} [E'_n(kb) T_{nm}^{24} \\ & - iG_2 E_n(kb) T_{nm}^{24} - E_n(kb) T_{nm}^{22}] + \sum_{n=0}^{\infty} C_n H_n(kb) [T_{nm}^{21} + iG_2 T_{nm}^{23}] + \sum_{n=1}^{\infty} D_n H_n(kb) [T_{nm}^{22} + iG_2 T_{nm}^{24}] = 0, \quad m = 0, 1, 2, \dots, \end{aligned} \tag{25c}$$

$$\begin{aligned} & \sum_{n=0}^{\infty} A_n^{(2)} J_n(kb) [T_{nm}^{25} + iG_2 T_{nm}^{27}] + \sum_{n=0}^{\infty} A_n^{(3)} [E'_n(kb) T_{nm}^{27} - iG_2 E_n(kb) T_{nm}^{27} - E_n(kb) T_{nm}^{25}] + \sum_{n=1}^{\infty} B_n^{(2)} J_n(kb) [T_{nm}^{26} + iG_1 T_{nm}^{28}] + \sum_{n=1}^{\infty} B_n^{(3)} [E'_n(kb) T_{nm}^{28} \\ & - iG_2 E_n(kb) T_{nm}^{28} - E_n(kb) T_{nm}^{26}] + \sum_{n=0}^{\infty} C_n H_n(kb) [T_{nm}^{25} + iG_2 T_{nm}^{27}] + \sum_{n=1}^{\infty} D_n H_n(kb) [T_{nm}^{26} + iG_2 T_{nm}^{28}] = 0, \quad m = 1, 2, 3, \dots, \end{aligned} \tag{25d}$$

where

$$\begin{cases}
 T_{nm}^{(t1)} = \int_{\alpha_1+\gamma_1-2\pi}^{\alpha_1} \cos(m\theta) \cos(n\theta) d\theta; & T_{nm}^{(t2)} = \int_{\alpha_1+\gamma_1-2\pi}^{\alpha_1} \cos(m\theta) \sin(n\theta) d\theta, \\
 T_{nm}^{(t3)} = \int_{\alpha_1}^{\alpha_1+\gamma_1} \cos(m\theta) \cos(n\theta) d\theta; & T_{nm}^{(t4)} = \int_{\alpha_1}^{\alpha_1+\gamma_1} \cos(m\theta) \sin(n\theta) d\theta, \\
 T_{nm}^{(t5)} = \int_{\alpha_1+\gamma_1-2\pi}^{\alpha_1} \sin(m\theta) \cos(n\theta) d\theta; & T_{nm}^{(t6)} = \int_{\alpha_1+\gamma_1-2\pi}^{\alpha_1} \sin(m\theta) \sin(n\theta) d\theta, \\
 T_{nm}^{(t7)} = \int_{\alpha_1}^{\alpha_1+\gamma_1} \sin(m\theta) \cos(n\theta) d\theta; & T_{nm}^{(t8)} = \int_{\alpha_1}^{\alpha_1+\gamma_1} \sin(m\theta) \sin(n\theta) d\theta,
 \end{cases} \tag{26}$$

where $t = 1$ and $t = 2$ correspond to arc walls 1 and 2, respectively.

To obtain the hydrodynamic loads and wave run-ups, the potential coefficients must be determined. By solving a system of equations involving Eqs. (20) and (25), the potential coefficients $A_n^{(1)}, A_n^{(2)}, A_n^{(3)}, B_n^{(1)}, B_n^{(2)}, B_n^{(3)}, C_n$, and D_n can be obtained. The series is truncated after N , i.e., n is from 0 to N . To derive the potential coefficients, Eqs. (20) and (25) can be truncated to a finite set of equations with $4(2M + 1)$ potential coefficients (depending on the required numerical accuracy).

Once the velocity potentials are known, the subsequent physical quantities (e.g., pressure distribution, overturning moments, and relative wave height) can be instantly determined. By considering the dynamic free surface condition, the water wave elevation for the three regions can be evaluated as follows:

$$\eta^{(j)} = -\frac{1}{g} \frac{\partial \phi^{(j)}}{\partial t} \quad (z = h; j = 1, 2, 3). \tag{27}$$

In practical calculations, the maximum dimensionless wave run-up around the interior cylinder is denoted by $\bar{\eta}_{cyl}$, in which the dimensionless factor is H .

The wave forces (the subscript, arc 1, arc 2, and cyl denote arc wall 1, arc wall 2, and the interior cylinder, respectively) acting on the arc walls and interior cylinder along the orthogonal directions are as follows:

$$\begin{cases}
 \left\{ \begin{matrix} F_{arc1,x} \\ F_{arc1,y} \end{matrix} \right\} = - \int_0^h dz \int_{\alpha_1}^{\alpha_1+\gamma_1} [P^{(1)} - P^{(2)}] \Big|_{r=a} a \begin{cases} \cos(\theta) \\ \sin(\theta) \end{cases} d\theta = \begin{cases} \text{Re}(f_{arc1,x}) \\ \text{Re}(f_{arc1,y}) \end{cases},
 \end{cases} \tag{28}$$

$$\begin{cases}
 \left\{ \begin{matrix} F_{arc2,x} \\ F_{arc2,y} \end{matrix} \right\} = - \int_0^h dz \int_{\alpha_2}^{\alpha_2+\gamma_2} [P^{(2)} - P^{(3)}] \Big|_{r=b} b \begin{cases} \cos(\theta) \\ \sin(\theta) \end{cases} d\theta = \begin{cases} \text{Re}(f_{arc2,x}) \\ \text{Re}(f_{arc2,y}) \end{cases},
 \end{cases} \tag{29}$$

$$\begin{cases}
 \left\{ \begin{matrix} F_{cyl,x} \\ F_{cyl,y} \end{matrix} \right\} = - \int_0^h dz \int_0^{2\pi} [P^{(3)}] \Big|_{r=c} c \begin{cases} \cos(\theta) \\ \sin(\theta) \end{cases} d\theta = \begin{cases} \text{Re}(f_{cyl,x}) \\ \text{Re}(f_{cyl,y}) \end{cases},
 \end{cases} \tag{30}$$

where the hydrodynamic pressure can be obtained based on the Bernoulli equation

$$P^{(j)} = -\rho \frac{\partial \Phi^{(j)}}{\partial t} \quad (j = 1, 2, 3). \tag{31}$$

Furthermore, calculating the integrals in Eqs. (28)–(30) yields the following:

$$\begin{cases}
 f_{arc1,x} = -\frac{\rho g a H h}{\pi} \int_0^\infty A(k) e^{-ikc_0 t} \sum_{n=0}^\infty \left\{ \left[\beta_n \cos(n\beta) J_n(ka) + A_n^{(1)} H_n(ka) - A_n^{(2)} J_n(ka) - C_n H_n(ka) \right] T_{n1}^{(13)} \right. \\
 \left. + \left[\beta_n \sin(n\beta) J_n(ka) + B_n^{(1)} H_n(ka) - B_n^{(2)} J_n(ka) - D_n H_n(ka) \right] T_{n1}^{(14)} \right\} dk, \\
 f_{arc1,y} = -\frac{\rho g a H h}{\pi} \int_0^\infty A(k) e^{-ikc_0 t} \sum_{n=0}^\infty \left\{ \left[\beta_n \cos(n\beta) J_n(ka) + A_n^{(1)} H_n(ka) - A_n^{(2)} J_n(ka) - C_n H_n(ka) \right] T_{n1}^{(17)} \right. \\
 \left. + \left[\beta_n \sin(n\beta) J_n(ka) + B_n^{(1)} H_n(ka) - B_n^{(2)} J_n(ka) - D_n H_n(ka) \right] T_{n1}^{(18)} \right\} dk,
 \end{cases} \tag{32}$$

$$\begin{cases}
 f_{arc2,x} = -\frac{\rho g b H h}{\pi} \int_0^\infty A(k) e^{-ikc_0 t} \sum_{n=0}^\infty \left\{ \left[A_n^{(2)} J_n(kb) + C_n H_n(kb) - A_n^{(3)} E_n(kb) \right] T_{n1}^{(23)} + \left[B_n^{(2)} J_n(kb) + D_n H_n(kb) - B_n^{(3)} E_n(kb) \right] T_{n1}^{(24)} \right\} dk, \\
 f_{arc2,y} = -\frac{\rho g b H h}{\pi} \int_0^\infty A(k) e^{-ikc_0 t} \sum_{n=0}^\infty \left\{ \left[A_n^{(2)} J_n(kb) + C_n H_n(kb) - A_n^{(3)} E_n(kb) \right] T_{n1}^{(27)} + \left[B_n^{(2)} J_n(kb) + D_n H_n(kb) - B_n^{(3)} E_n(kb) \right] T_{n1}^{(28)} \right\} dk,
 \end{cases} \tag{33}$$

$$\begin{cases} f_{cyl,x} = -\rho g H c h \int_0^\infty A(k) e^{-ikc_0 t} A_1^{(3)} E_1(kc) dk, \\ f_{cyl,y} = -\rho g H c h \int_0^\infty A(k) e^{-ikc_0 t} B_1^{(3)} E_1(kc) dk. \end{cases} \quad (34)$$

The total wave forces on the two walls and the interior cylinder can be written as follows:

$$\begin{cases} F_{arc1} = \sqrt{(F_{arc1,x})^2 + (F_{arc1,y})^2}, \\ F_{arc2} = \sqrt{(F_{arc2,x})^2 + (F_{arc2,y})^2}, \\ F_{cyl} = \sqrt{(F_{cyl,x})^2 + (F_{cyl,y})^2}. \end{cases} \quad (35)$$

In addition, dimensionless factors $\rho g H a h$, $\rho g H b h$, and $\rho g H c h$ are employed to determine the dimensionless wave forces acting on arc 1, arc 2, and the interior cylinder, respectively. Here, the symbols $|\bar{F}_{arc1}|$, $|\bar{F}_{arc2}|$, and $|\bar{F}_{cyl}|$ denote the maximum dimensionless hydrodynamic loads acting on arc 1, arc 2, and the interior cylinder, as follows:

$$|\bar{F}_{arc1}| = \frac{F_{arc1}^{max}}{\rho g H a h}, \quad |\bar{F}_{arc2}| = \frac{F_{arc2}^{max}}{\rho g H b h}, \quad |\bar{F}_{cyl}| = \frac{F_{cyl}^{max}}{\rho g H c h}, \quad (36)$$

where F_{arc1}^{max} , F_{arc2}^{max} , and F_{cyl}^{max} denote the amplitudes of the corresponding F_{arc1} , F_{arc2} , and F_{cyl} respectively.

In practice, for shallow water waves, a simple linear relationship between the overturning moment and wave loads exists (i.e., the overturning moment acting on the structure is exactly half of the corresponding force, indicating that they are experiencing similar changes). Moreover, because the wavelength of a solitary wave is infinite, the wave diffraction parameter kh tends to zero and becomes unimportant. Nevertheless, diffraction is a key feature of wave–structure interactions (Sankarababu *et al.*, 2008). Thus, to describe the diffraction characteristics of solitary waves, parameter $\chi = \sqrt{Hc^2/h^3}$ was introduced (Isaacson, 1983).

III. MODEL VALIDATION

To validate the present analytical model, the present numerical results are compared with a number of published results. When $\gamma_1 = 2\pi$ and $G_1 = 0$, the current structure transforms into an impermeable cylinder. The hydrodynamic loads on an impermeable cylinder obtained by the present study and the work of Isaacson (1983) are shown in Fig. 3: (a) is the plot of non-dimensional wave forces with the corresponding time $\sqrt{gH}t/h$ for different values of $\bar{\chi}$ ($\bar{\chi} = \sqrt{Ha^2/h^3}$), and (b) is the plot of non-dimensional wave forces with the wave parameter $\bar{\chi}$. When $\gamma_1 = 2\pi$, $\gamma_2 = 0$, and $c = 0$, the current structure becomes a permeable cylinder. The hydrodynamic loads on a permeable cylinder for different wave-porous parameters obtained by the present study and the work of Basmat (2002) are shown in Fig. 4: (a) $\bar{\chi} = 1$, $a = 1$ m and (b) $\bar{\chi} = 2$, $a = 2$ m. Excellent agreement between the present results and the published data (Figs. 3 and 4) gives confidence in the present model for solving the problem of solitary waves interaction with a combined structure of two concentric porous arc walls.

IV. NUMERICAL RESULTS AND DISCUSSION

To investigate the effects of different parameters on the hydrodynamic performance of solitary waves using the structure considered in this work, a numerical calculation program was developed based on the formulas derived in this study. To facilitate the illustration of the distance of arc 2 from arc 1 and from the cylinder, a new parameter, $\lambda = (b - c)/(a - c)$, is introduced. Note that the purpose of this study is to investigate the effect of different parameters on the interior cylinder that must be protected and provide reference for future practical engineering design. As computational examples, the radius of arc wall 1 is set to $a = 40$ m, the radius of the interior cylinder is $c = 20$ m, and the wave height is $H = 1$ m. Notably, since the water height H and the radius of the interior cylinder c are constants, the water depth h can be calculated for different diffraction parameters χ according to the formula $h = (Hc^2/\chi^2)^{1/3}$.

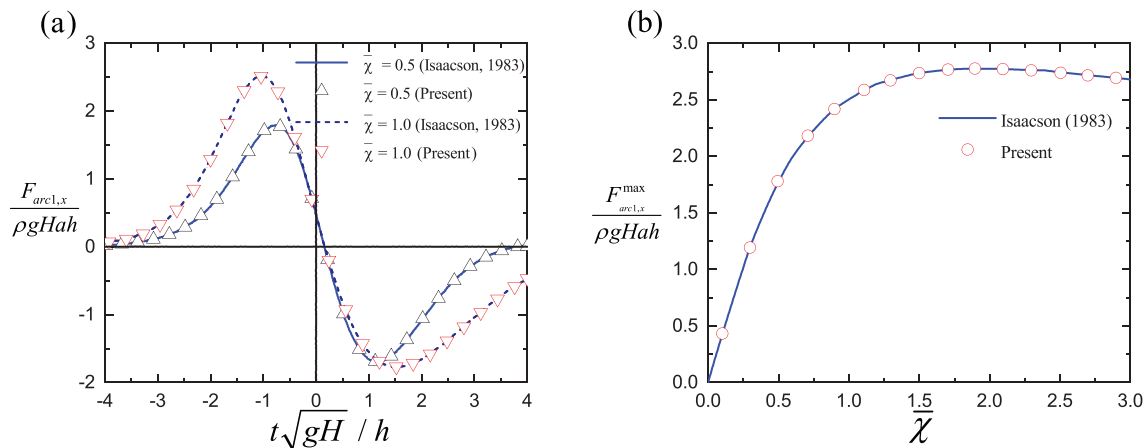


FIG. 3. Comparison of the dimensionless wave force on an impermeable cylinder with $G_1 = 0$, $\gamma_1 = 2\pi$, and $\beta = 0$: (a) plot of non-dimensional wave forces with the corresponding time $\sqrt{gH}t/h$ for different values of $\bar{\chi}$ and (b) plot of non-dimensional wave forces with the wave parameter $\bar{\chi}$.

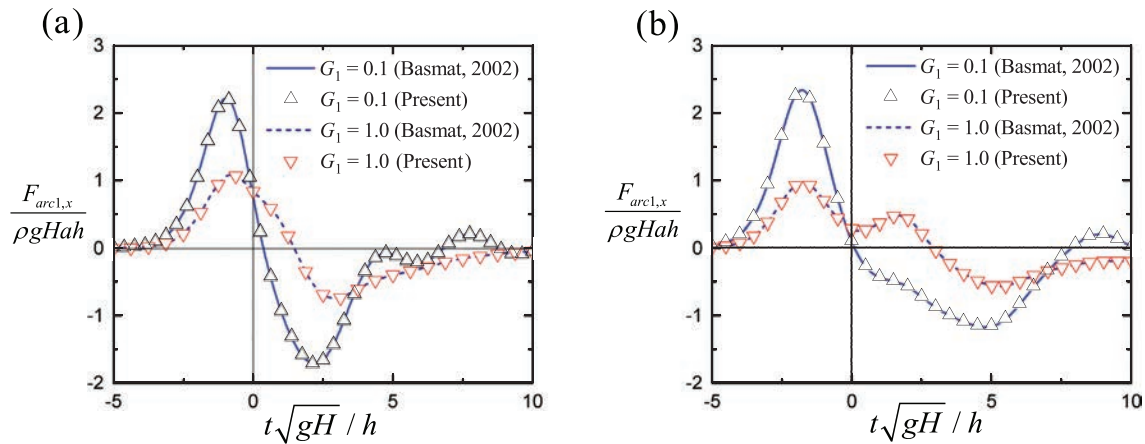


FIG. 4. Comparison of the dimensionless wave force on a porous cylinder vs corresponding time $\sqrt{gH}t/h$ for various values of G_1 with $\gamma_1 = 2\pi$, $\gamma_2 = 0$, $c = 0$, and $\beta = 0$: (a) $\bar{\chi} = 1$, $a = 1$ m and (b) $\bar{\chi} = 2$, $a = 2$ m.

A. Effect of arc wall 2 location

Figure 5 shows the influence of the location of arc wall 2 on the force $|\bar{F}_{cyl}|$ and run-up $\bar{\eta}_{cyl}$ on the solid cylinder with $\gamma_1 = \gamma_2 = 2\pi/3$, $\alpha_1 = \alpha_2 = 2\pi/3$, $G_1 = G_2 = 1$, $\beta = 0$, and $c/a = 0.5$. As shown in Fig. 5(a), for the different λ , the force acting on the cylinder first monotonically increases to a maximum around $\chi = 1.2$ and then decreases gradually with increasing χ . When $\lambda > 0.4$, the force on the interior cylinder does not change much for different λ . In addition, the wave force marginally increases when λ increases from 0.6 to 0.8. This occurs because not enough physical space remains for the solitary waves transmitted into the annular region between arc walls 1 and 2 to develop, partially preventing the wave passage through the annular region and the direct interaction with the cylinder. As indicated in Fig. 5(b), the wave run-up around the cylinder monotonically decreases with increasing λ . This is because when arc 2 moves toward arc 1, the protection area of arc 2 expands with its radius providing a

smoother water area for the cylinder. The peak and trough values of wave run-up occur at $\theta/\pi \approx 0.2$ and 0.6 , respectively. Moreover, the main peak of the wave run-up curves slightly moves toward the smaller θ with increasing λ .

B. Effect of wave incident angle

Figure 6 illustrates the influence of the incident angle on the force $|\bar{F}_{cyl}|$ and run-up $\bar{\eta}_{cyl}$ on the solid cylinder with $\gamma_1 = \gamma_2 = 2\pi/3$, $\alpha_1 = \alpha_2 = 2\pi/3$, $G_1 = G_2 = 1$, $\lambda = 0.5$, and $c/a = 0.5$. As shown in Fig. 6(a), the hydrodynamic forces on the cylinder increase to a peak and then decrease gradually with increasing χ . As β increases, the wave loads acting on the cylinder gradually increase. This is because as β increases, part of the wave is not affected by arc walls 1 and 2; however, this partial wave directly impinges on the cylinder. In other words, the protection of the cylinder provided by the two arc walls gradually diminishes. This means that the use of arc structures to

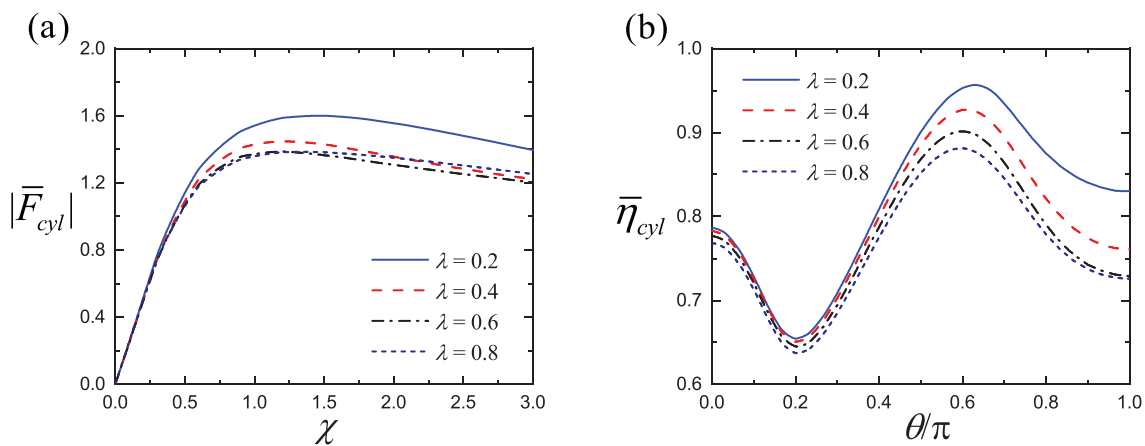


FIG. 5. Variation of the non-dimensional wave force and run-up on the solid cylinder for different values of λ with $\gamma_1 = \gamma_2 = 2\pi/3$, $\alpha_1 = \alpha_2 = 2\pi/3$, $\beta = 0$, $G_1 = G_2 = 1$, and $c/a = 0.5$: (a) wave force and (b) wave run-up, $\chi = 1$.

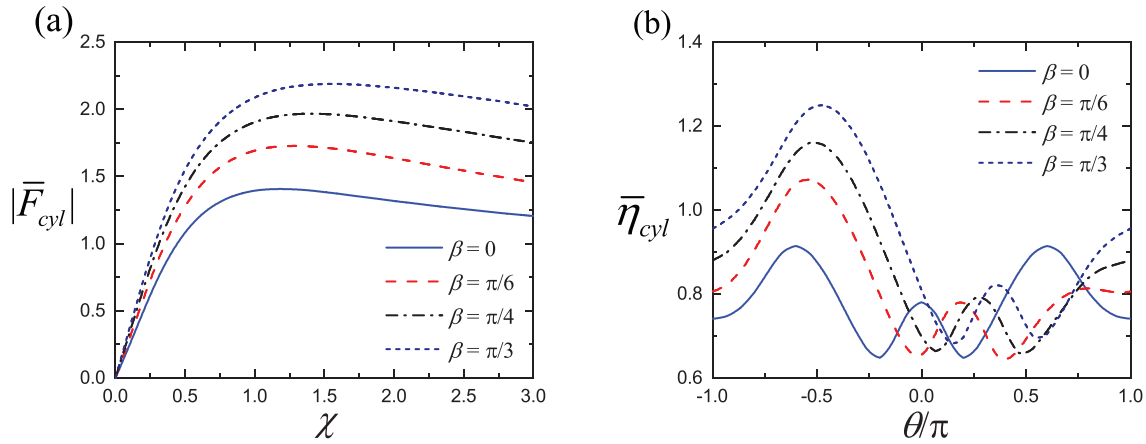


FIG. 6. Variation of the non-dimensional wave force and run-up on the solid cylinder for different values of β with $\gamma_1 = \gamma_2 = 2\pi/3$, $\alpha_1 = \alpha_2 = 2\pi/3$, $G_1 = G_2 = 1$, $\lambda = 0.5$, and $c/a = 0.5$: (a) wave force and (b) wave run-up, $\chi = 1$.

protect offshore structures must suit the particular environment, i.e., the direction of incoming waves is relatively stable. In Fig. 6(b), when $\beta > 0$, the wave run-up around the cylinder loses its symmetry about the x -axis; it distinctly increases with β , which is the same reason for the increase in wave loads. The approximate maximum values of wave run-up occur around $\theta/\pi = -0.5$, and the main peak of the $\bar{\eta}_{cyl} - \theta$ curve gradually moves toward the large θ with increasing β , owing to the position shift where the wave directly impinges on the cylinder.

C. Effect of porous-effect parameters

In this section, the real physical meaning of the porous-effect parameter is visually described to improve reader understanding. The porous-effect parameter is related to the density and radii of thin-walled holes, indicating that, for the same pressure jump across the porous arc wall, the more densely packed holes and larger hole radii, the larger the radial flow velocity of the fluid passing across the wall.

Figure 7 shows the influence of the porous-effect parameters, G_1 and G_2 on the force $|\bar{F}_{cyl}|$ on the solid cylinder for different β values with $\gamma_1 = \gamma_2 = 2\pi/3$, $\alpha_1 = \alpha_2 = 2\pi/3$, $\lambda = 0.5$, $\chi = 1$, and $c/a = 0.5$. Figure 7(a) shows that, as G_1 increases, the force acting on the cylinder monotonically increases toward its asymptotic value. Moreover, the larger value of β , the larger is the value of the wave force acting on the interior cylinder. As β increases, $|\bar{F}_{cyl}|$ turns insensitive to the change of G_1 . A similar observation is presented in Fig. 7(b). The force acting on the cylinder first slightly decreases and then monotonically increases, indicating that there is an optimal G_2 value that can reduce the wave force on the interior cylinder. As shown in Fig. 7(b), an inflection point occurs in the wave load acting on the interior cylinder. When arc wall 2 is transformed from an impermeable structure to a permeable structure, the surge waves formed in region 3 begin to flow through the permeable arc wall 2 into region 2, which causes a reduction in wave elevation in region 3. Physically, the hydrodynamic forces acting on the interior cylinder are related to the pressure difference

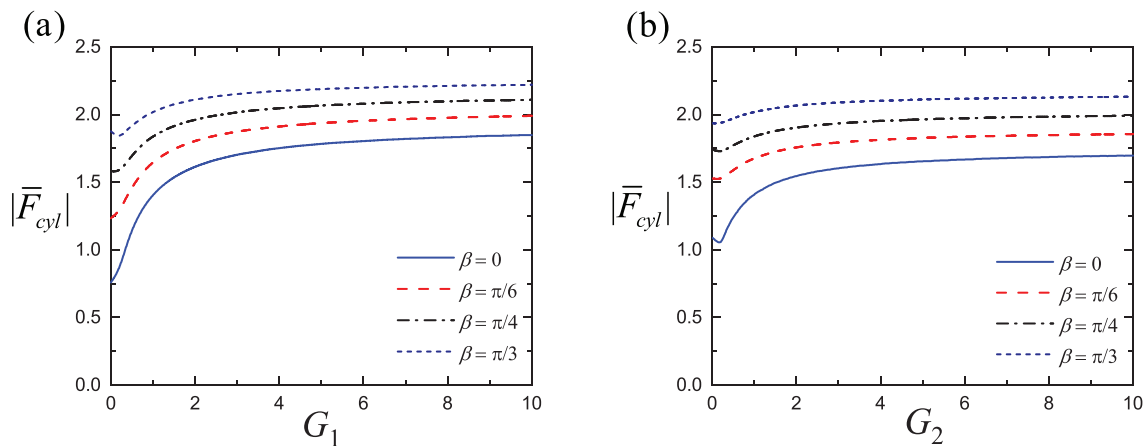


FIG. 7. Variation of the non-dimensional wave force on the cylinder for different values of β with $\gamma_1 = \gamma_2 = 2\pi/3$, $\alpha_1 = \alpha_2 = 2\pi/3$, $\chi = 1$, $\lambda = 0.5$, and $c/a = 0.5$: (a) $G_2 = 1$ and (b) $G_1 = 1$.

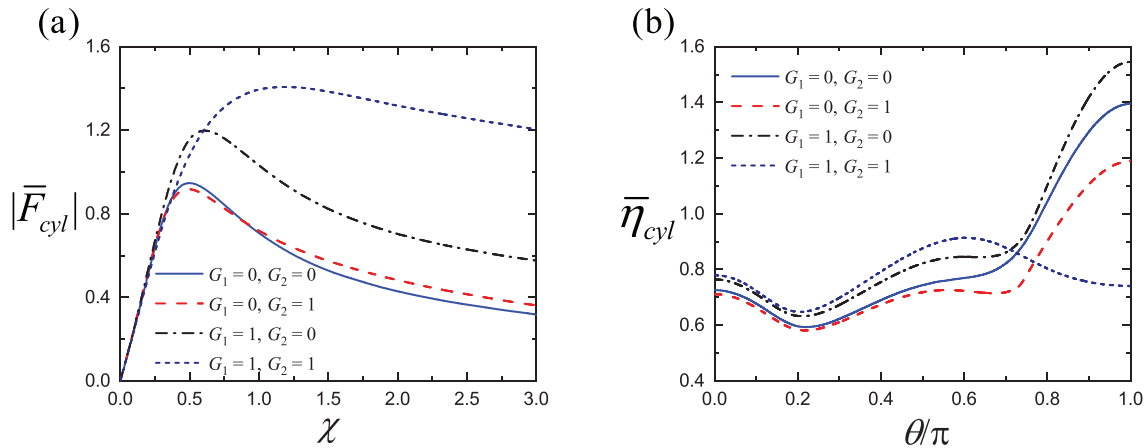


FIG. 8. Variation of the non-dimensional wave force and run-up on the cylinder for different values of G_1 and G_2 with $\gamma_1 = \gamma_2 = 2\pi/3$, $\alpha_1 = \alpha_2 = 2\pi/3$, $\lambda = 0.5$, and $\beta = 0$: (a) wave force and (b) wave run-up, $\chi = 1$.

around the body, i.e., when the pressure difference between the windward and leeward side of the cylinder decreases, the wave load also decreases. However, with the increase in G_2 , the protective effect of arc wall 2 on the interior cylinder gradually disappears, leading to a gradual increase in the wave run-up around the windward side of the body, i.e., the wave loads gradually increase.

Because arc walls 1 and 2 can adapt to different porous-effect coefficients, the discussion of the situation in which both impermeable and permeable arcs exist is necessary. Thus, four typical combinations of porous-effect permeability factors are selected to compare the effectiveness of protection for the interior cylinder. These factors are as follows: (1) $G_1 = G_2 = 0$, both arc walls are impermeable; (2) $G_1 = 0$, $G_2 = 1$, arc 1 is impermeable, and arc 2 is permeable; (3) $G_1 = 1$, $G_2 = 0$, arc 1 is permeable, and arc 2 is impermeable; (4) $G_1 = G_2 = 1$, both arc walls are permeable. Figure 8 shows $|\bar{F}_{cyl}| - \chi$ and $\bar{\eta}_{cyl} - \theta$ with $\chi = 1$ for the four combinations of porous-effect parameters with $\gamma_1 = \gamma_2 = 2\pi/3$, $\alpha_1 = \alpha_2 = 2\pi/3$, $\lambda = 0.5$, and $c/a = 0.5$. As shown in Fig. 8(a), the $|\bar{F}_{cyl}| - \chi$ curves for $G_2 = 0$ and 1 nearly overlap with one another, indicating that the wave forces acting on the interior cylinder are insensitive to the porosity of arc 2. However, once arc 1 is permeable, it becomes apparent that whether arc 2 is permeable or not has a significant effect on the wave forces on the cylinder. This shows that arc 1 plays a greater role in protecting the cylinder than arc 2. As shown in Fig. 8(b), the wave run-ups around the cylinder become more complex for the four cases. On the leeward side of the cylinder, the wave run-up only slightly changes for the four cases, whereas on the windward side of the cylinder, remarkable changes in the amplitude of wave run-up can be observed. To illustrate this phenomenon, the changes in the relative wave height near the combined structure as G_1 and G_2 varies are shown in Fig. 9. The calculation conditions are the same as those shown in Fig. 8(b). As illustrated in Figs. 9(a) and 9(b), the amplitude of the relative wave height around arc 1 is extremely large with a possible risk of overtopping. Furthermore, as shown in Figs. 9(a) and 9(c), the amplitude of the relative wave height around the cylinder is also extremely high, even higher than that of a single cylinder without exterior wall protection. This is possibly because both arc 2 and the cylinder are

impermeable and wave resonance is likely to happen at the region between arc 2 and the cylinder. In other words, gap resonance may occur in region 2 when the annular spacing between arc 2 and the interior cylinder is small, e.g., $c/b > 0.5$, and the arc 2 is impermeable ($G_2 = 0$). The waves come from both ends of the channel between arc 2 and the cylinder aggregate to form a surge inside the channel. When both arc 1 and arc 2 are permeable [i.e., $G_1 = G_2 = 1$, see Fig. 9(d)], the possible resonance among solid structures as observed in Figs. 9(a)–9(c), particularly Figs. 9(a) and 9(c), disappears. A relatively still water environment is created between the arc walls and cylinder, demonstrating the effectiveness of permeable structures in protecting the interior cylinder.

D. Effect of opening angles of two arc walls

The influence of the opening angles γ_1 and γ_2 on the force $|\bar{F}_{cyl}|$ on the solid cylinder for different values of β with $\lambda = 0.5$, $\chi = 1$, and $c/a = 0.5$ is shown in Fig. 10, (a) $\alpha_1 = \pi - \gamma_1/2$, $\alpha_2 = \gamma_2 = 2\pi/3$, and (b) $\alpha_2 = \pi - \gamma_2/2$, $\alpha_1 = \gamma_1 = 2\pi/3$, respectively. As expected, a clear trend of gradually decreasing wave force on the cylinder with increasing γ_1 or γ_2 is observed. This is because the large opening angle provides a large sheltered area for the interior cylinder. Moreover, the wave force on the cylinder is virtually constant after the opening angle exceeds a specific value. For instance, when $\gamma_1/\pi > 0.8$, the force acting on the cylinder remains virtually the same for $\beta = 0$. In addition, the rate at which the wave force reaches its asymptotic value gradually decelerates; it increases in amplitude with β .

Because the opening angles of both arc walls 1 and 2 can be modified, a multiplicity of structural configurations can be formed. Two special cases are selected to be studied and discussed separately. Case (1) involves the comparison of the hydrodynamic performance of a single cylinder ($\gamma_1 = \gamma_2 = 0$), a cylinder with an arc outer wall ($\gamma_1 = 2\pi/3$, $\gamma_2 = 0$), and a cylinder with dual-arc outer walls ($\gamma_1 = \gamma_2 = 2\pi/3$). Case (2) considers the comparison of the hydrodynamic performance of a single cylinder ($\gamma_1 = \gamma_2 = 0$), a cylinder with a concentric outer wall ($\gamma_1 = 2\pi$, $\gamma_2 = 0$), and a cylinder with two concentric outer walls ($\gamma_1 = \gamma_2 = 2\pi$). The force $|\bar{F}_{cyl}|$ and run-up

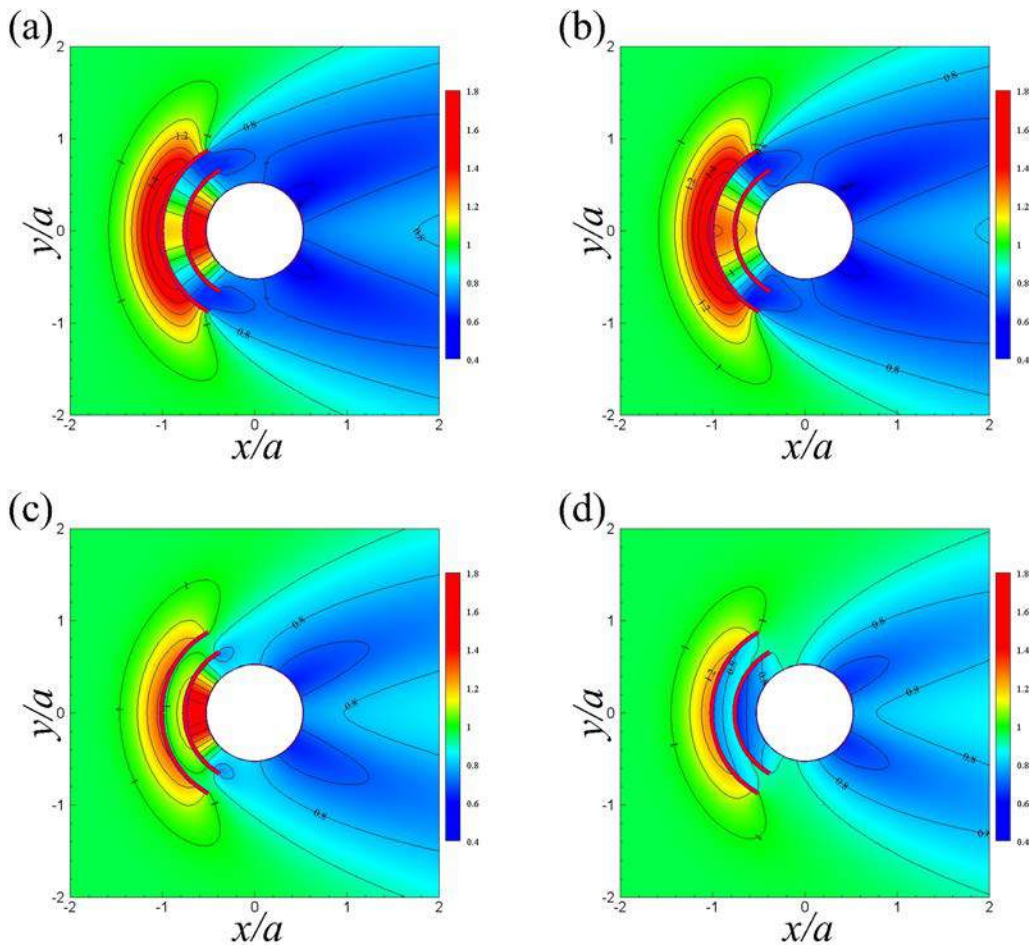


FIG. 9. Distribution of the relative wave height for different values of G_1 and G_2 with $\beta = 0$, $\chi = 1$, $\alpha_1 = \alpha_2 = 2\pi/3$, $\gamma_1 = \gamma_2 = 2\pi/3$, $\lambda = 0.5$, and $c/a = 0.5$: (a) $G_1 = 0$, $G_2 = 0$, (b) $G_1 = 0$, $G_2 = 1$, (c) $G_1 = 1$, $G_2 = 0$, and (d) $G_1 = 1$, $G_2 = 1$.

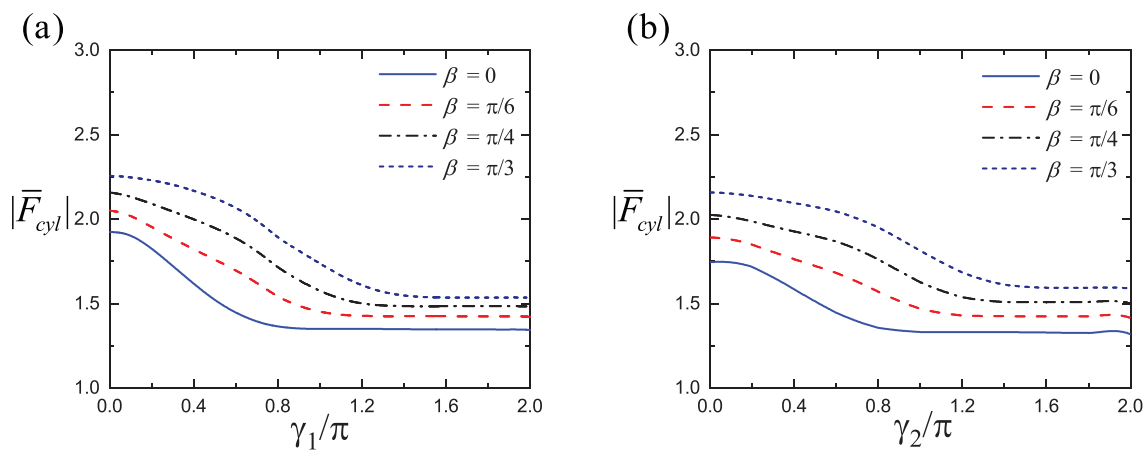


FIG. 10. Variation of dimensionless wave forces on the exterior and interior arc-shaped walls for different values of β with $G_1 = G_2 = 1$, $\lambda = 0.5$, $c/a = 0.5$, and $\chi = 1$: (a) $\alpha_1 = \pi - \gamma_1/2$, $\alpha_2 = \gamma_2 = 2\pi/3$ and (b) $\alpha_2 = \pi - \gamma_2/2$, $\alpha_1 = \gamma_1 = 2\pi/3$.

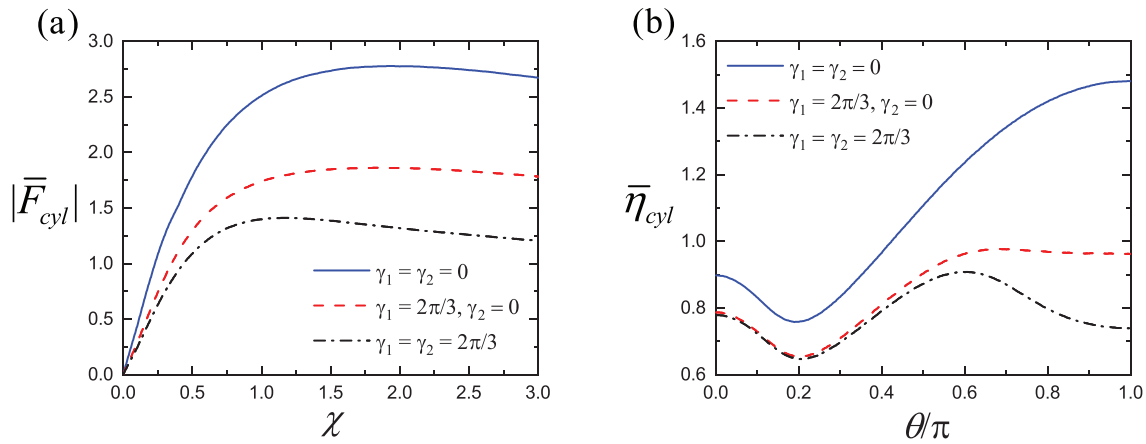


FIG. 11. Comparison wave force and run-up on the solid cylinder for three kinds of structure for the case (1) with $\lambda = 0.5$, $c/a = 0.5$, and $\beta = 0$: (a) wave force and (b) wave run-up, $\chi = 1$.

$\bar{\eta}_{cyl}$ on the solid cylinder for case (1) with $\alpha_1 = \alpha_2 = 2\pi/3$, $G_1 = G_2 = 1$, $\beta = 0$, $\lambda = 0.5$, and $c/a = 0.5$ are shown in Fig. 11, (a) wave force and (b) wave run-up ($\chi = 1$), respectively. As shown in Fig. 11(a), for case (1) of the three different configurations, the peak values of the force on the interior cylinder are 2.77, 1.86, and 1.41. In other words, the amplitude of the wave force decreases by approximately 33% and 49% for the single-arc and dual-arc walls, respectively. As shown in Fig. 11(b), for the cylinder with dual-arc walls, the wave run-up on the windward side has a more significant decline than that of the single-arc structure. However, the wave run-up on the leeward side virtually does not change for the single-arc and dual-arc structures. The relative wave height variation around the combined structure for case (1) is shown in Fig. 12; the calculation conditions are the same as those shown in Fig. 12(b). The comparison of the relative elevations in case (1) intuitively shows that the wave surface around the cylinder protected by the single-arc or dual-arc structure becomes flat. Moreover, due to the existence of arc 2, further reduction in the wave height around the cylinder is observed. The force $|\bar{F}_{cyl}|$ and run-up $\bar{\eta}_{cyl}$ on the solid cylinder for case (2) with $\alpha_1 = \alpha_2 = 0$, $G_1 = G_2 = 1$, $\beta = 0$, $\lambda = 0.5$, and $c/a = 0.5$ are shown in Fig. 13, (a) wave force, and (b) wave run-up ($\chi = 1$), respectively. As shown in

Fig. 13(a), for case (2) of the three different configurations, the maximum values of the force on the interior cylinder are 2.77, 1.85, and 1.32. This means that the wave force amplitude decreases by approximately 33% and 52% for the single outer wall and dual outer walls, respectively. Interestingly, for the normal incident wave ($\beta = 0$), the single-arc and single concentric walls (or dual-arc and dual concentric outer walls) are considerably similar in terms of protecting the interior cylinder. In Fig. 13(b), on the windward side, a similar trend of wave run-ups shown in Fig. 11(b) can be observed. However, on the leeward side, the wave run-up occurs in the opposite trend with the increase in the number of outer walls; this occurs because the waves are reflected by arc 1. The relative wave height variation around the combined structure for case (2) is shown in Fig. 14; the calculation conditions are the same as those shown in Fig. 13(b). Clearly, the dual cylindrical walls provide better protection to the cylinder than the single cylindrical wall, indicating that a cylinder with dual cylindrical walls can deal with more complex marine environments.

E. Effect of orientation of arc walls 1 and 2

The influence of the orientation of arcs 1 and 2 on the force $|\bar{F}_{cyl}|$ on the solid cylinder for different β values with $\gamma_1 = \gamma_2 = 2\pi/3$,

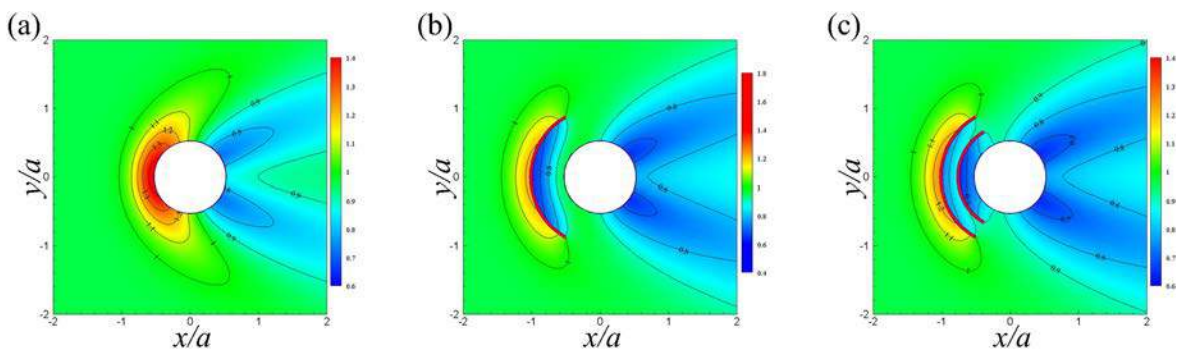


FIG. 12. Distribution of the relative wave height for case (1) with $\beta = 0$, $\chi = 1$, $\lambda = 0.5$, $G_1 = G_2 = 1$, and $c/a = 0.5$: (a) $\gamma_1 = \gamma_2 = 0$; (b) $\alpha_1 = 2\pi/3$, $\gamma_1 = 2\pi/3$, $\gamma_2 = 0$; and (c) $\alpha_1 = \alpha_2 = 2\pi/3$, $\gamma_1 = \gamma_2 = 2\pi/3$.

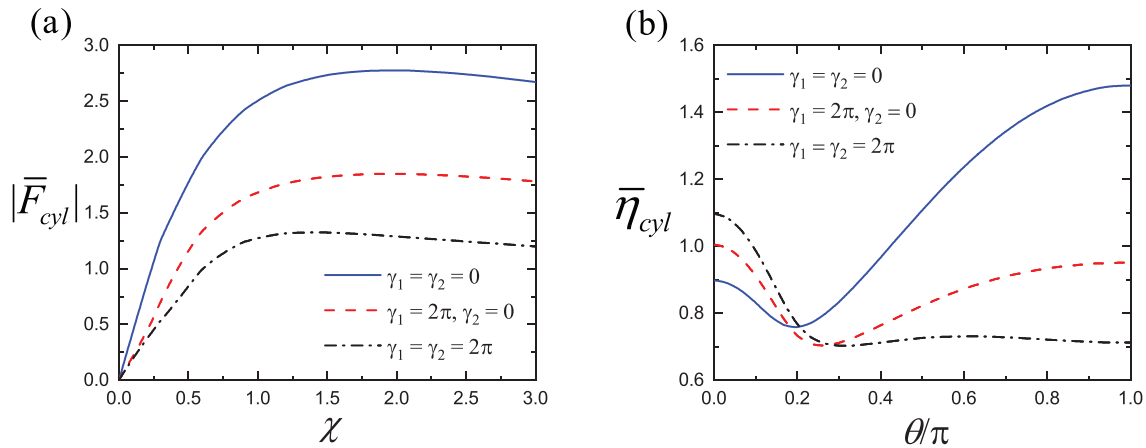


FIG. 13. Comparison wave force and run-up on the solid cylinder for three kinds of structure for the case (2) with $\gamma_1 = \gamma_2 = 2\pi/3$, $\alpha_1 = \alpha_2 = 2\pi/3$, $\lambda = 0.5$, and $\beta = 0$: (a) $G_2 = 1$ and (b) $\lambda = 1$.

$\lambda = 0.5$, $\chi = 1$, and $c/a = 0.5$ is shown in Fig. 15, (a) $\alpha_2 = 2\pi/3$ and (b) $\alpha_1 = 2\pi/3$, respectively. The figure clearly shows that when α_1 or α_2 decreases from $2\pi/3$ to $-\pi/3$, the position of arc 1 or arc 2 is rotated from being symmetrically oriented on the negative half-axis of the x -axis to being symmetrically placed about the positive half-axis of the x -axis. In Fig. 15(a), with decreasing α_1 , the magnitude of the wave force acting on the cylinder gradually increases. This is because the interior cylinder has switched from being protected by dual-arc walls to being protected by a single-arc wall. A similar phenomenon can be observed in Fig. 15(b), in which the wave load is not expected to vary considerably when $\alpha_2 < \pi/3$. The relative wave height variation around the combined structure for varying α_1 and α_2 with $\beta = 0$, $\chi = 1$, $\gamma_1 = \gamma_2 = 2\pi/3$, $\lambda = 0.5$, $G_1 = G_2 = 1$, and $c/a = 0.5$ is shown in Fig. 16, (a) $\alpha_1 = 2\pi/3$, $\alpha_2 = \pi/6$, (b) $\alpha_1 = 2\pi/3$, $\alpha_2 = 0$, (c) $\alpha_1 = 2\pi/3$, $\alpha_2 = -\pi/3$, (d) $\alpha_2 = 2\pi/3$, $\alpha_1 = \pi/6$, (e) $\alpha_2 = 2\pi/3$, $\alpha_1 = 0$, and (f) $\alpha_2 = 2\pi/3$, $\alpha_1 = -\pi/3$. The figure shows that the wave patterns become more complex when the two arc walls are not symmetrical about the x -axis. Moreover, the rotation of arc 1 has a more significant impact on the wave field around the structure than that of arc 2. This is because arc 1 provides a larger sheltered area than arc 2;

this is attributed to the relatively stable water environment provided by the presence of arc 1, which greatly diminishes the effect on the overall wave field when arc 2 is rotated [Figs. 16(d) and 16(e)].

Although the asymmetrical placement of the arc structures renders, these arcs are less effective in protecting the interior cylinder, and the area protected by the arc walls is extended. In practical engineering, the area of intersection between the two arcs can be applied as a channel for ship navigation. Thus, the study of this cross-distributed structure has considerable engineering value. Here, two typical cases are selected to investigate the hydrodynamic performance of cross-distributed structures. Case (1) consider the comparison of the hydrodynamic performance of a cylinder with a single-arc wall ($\alpha_1 = 2\pi/3$, $\gamma_1 = 2\pi/3$, $\gamma_2 = 0$), a cylinder with two crossed-arc outer walls ($\alpha_1 = 2\pi/3$, $\gamma_1 = \pi/2$, $\alpha_2 = \pi$, $\gamma_2 = \pi/3$), and a cylinder with two uncrossed-arc outer walls ($\alpha_1 = 2\pi/3$, $\gamma_1 = \pi/3$, $\alpha_2 = \pi$, $\gamma_2 = \pi/3$). Case (2) involves the comparison of the hydrodynamic performance of a cylinder with a single-arc wall ($\alpha_1 = \pi/2$, $\gamma_1 = \pi$, $\gamma_2 = 0$), a cylinder with two crossed-arc outer walls ($\alpha_1 = \pi/2$, $\gamma_1 = 2\pi/3$, $\alpha_2 = \pi$, $\gamma_2 = \pi/2$), and a cylinder with two uncrossed-arc outer walls ($\alpha_1 = \pi/2$, $\gamma_1 = \pi/2$, $\alpha_2 = \pi$, $\gamma_2 = \pi/2$). The force $|F_{cyl}|$ and run-up $\bar{\eta}_{cyl}$ on the solid cylinder

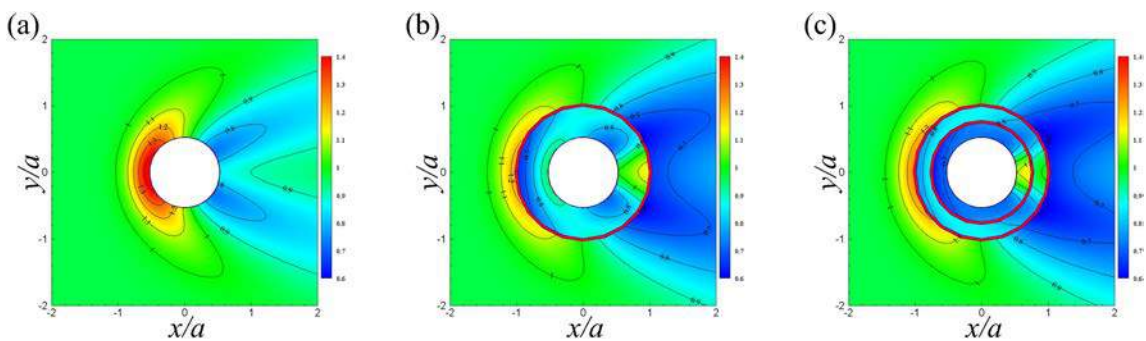


FIG. 14. Distribution of the relative wave height for case (2) with $\beta = 0$, $\chi = 1$, $\lambda = 0.5$, $G_1 = G_2 = 1$, and $c/a = 0.5$: (a) $\gamma_1 = \gamma_2 = 0$; (b) $\alpha_1 = 0$, $\gamma_1 = 2\pi$, $\gamma_2 = 0$; and (c) $\alpha_1 = \alpha_2 = 0$, $\gamma_1 = \gamma_2 = 2\pi$.

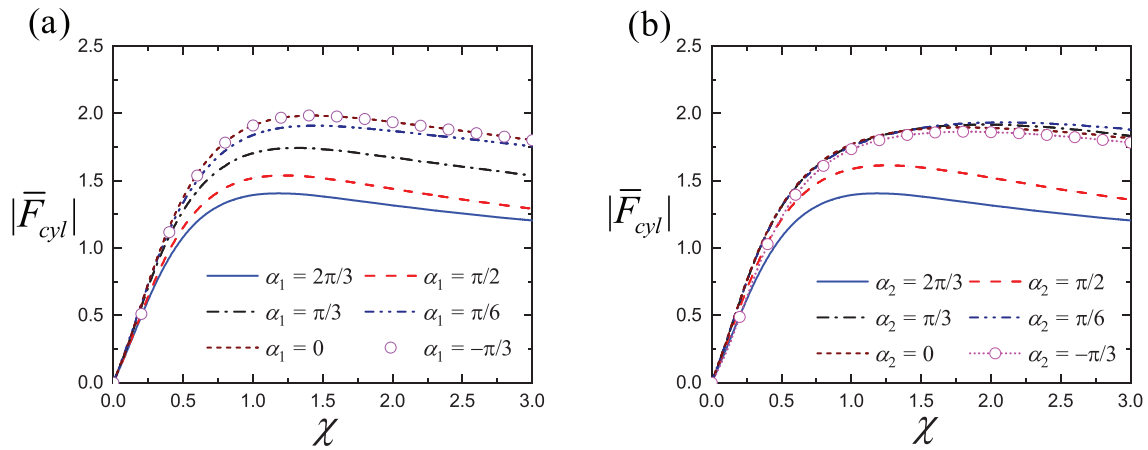


FIG. 15. Variation of the non-dimensional wave force on the cylinder for different values of $\alpha_1(\alpha_2)$ with $\gamma_1 = \gamma_2 = 2\pi/3$, $G_1 = G_2 = 1$, $\lambda = 0.5$, $c/a = 0.5$, and $\beta = 0$: (a) $\alpha_2 = 2\pi/3$ and (b) $\alpha_1 = 2\pi/3$.

for case (1) with $\beta = 0$, $\lambda = 0.5$, and $c/a = 0.5$ are shown in Fig. 17, (a) wave force and (b) wave run-up ($\chi = 1$). Figure 17(a) indicates that the wave forces acting on the interior cylinder with a single-arc are close to those acting on the interior cylinder with two crossed arcs. Nevertheless, the wave forces acting on both cylinders with a single-arc are significantly smaller than that acting on the cylinder with two uncrossed arcs. Moreover, an analogous phenomenon of wave run-up on the cylinder can also be observed in Fig. 17(b). This may indicate

that a configuration with a cylinder having two crossed arcs is a viable option. In contrast, caution is required in using a configuration with a cylinder having two uncrossed arcs. The relative wave height change near the combined structure for case (1) is shown in Fig. 18; the calculation conditions are the same as those shown in Fig. 17(b). The wave field of a cylinder with two crossed arcs is more complex than that of a cylinder with a single-arc, whereas the overall wave height amplitude in the wave region does not considerably vary. However, the wave

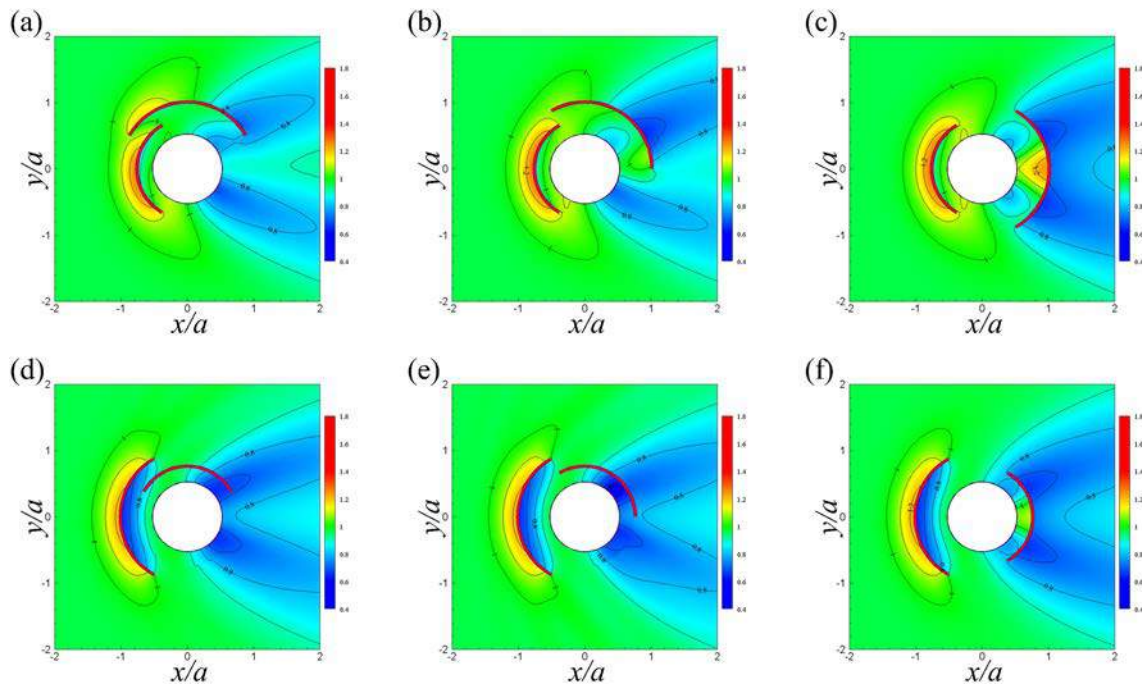


FIG. 16. Distribution of the relative wave height for different orientations of arcs 1 and 2 with $\beta = 0$, $\chi = 1$, $\gamma_1 = \gamma_2 = 2\pi/3$, $\lambda = 0.5$, $G_1 = G_2 = 1$, and $c/a = 0.5$: (a) $\alpha_1 = 2\pi/3$, $\alpha_2 = \pi/6$, (b) $\alpha_1 = 2\pi/3$, $\alpha_2 = 0$, (c) $\alpha_1 = 2\pi/3$, $\alpha_2 = -\pi/3$, (d) $\alpha_2 = 2\pi/3$, $\alpha_1 = \pi/6$, (e) $\alpha_2 = 2\pi/3$, $\alpha_1 = 0$, and (f) $\alpha_2 = 2\pi/3$, $\alpha_1 = -\pi/3$.

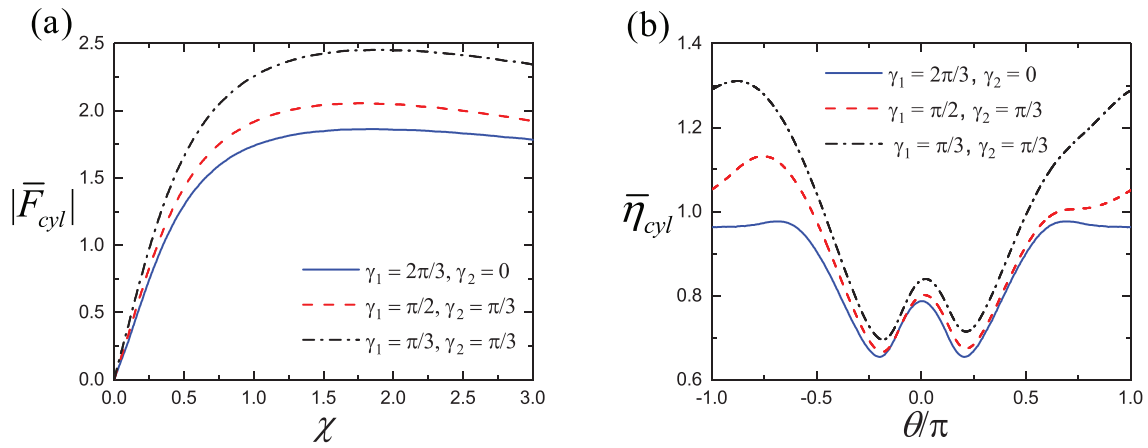


FIG. 17. Variation of the non-dimensional wave force and run-up on the cylinder for three kinds of structure for case 1 with $\alpha_1 = 2\pi/3, \alpha_2 = \pi, \lambda = 0.5, c/a = 0.5$, and $\beta = 0$: (a) wave force and (b) wave run-up, $\chi = 1$.

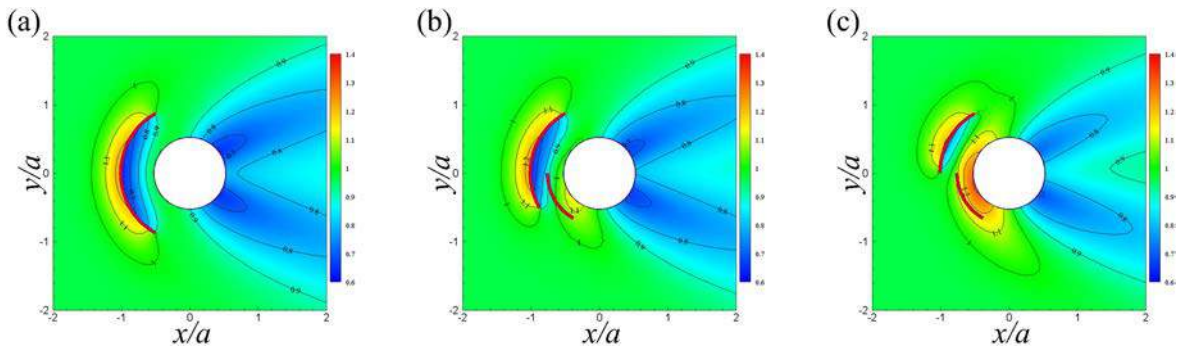


FIG. 18. Distribution of the relative wave height for case 1 with $\beta = 0, \chi = 1, \alpha_1 = 2\pi/3, \alpha_2 = \pi, \lambda = 0.5, G_1 = G_2 = 1$, and $c/a = 0.5$: (a) $\gamma_1 = 2\pi/3, \gamma_2 = 0$, (b) $\gamma_1 = \pi/2, \gamma_2 = \pi/3$, and (c) $\gamma_1 = \pi/3, \gamma_2 = \pi/3$.

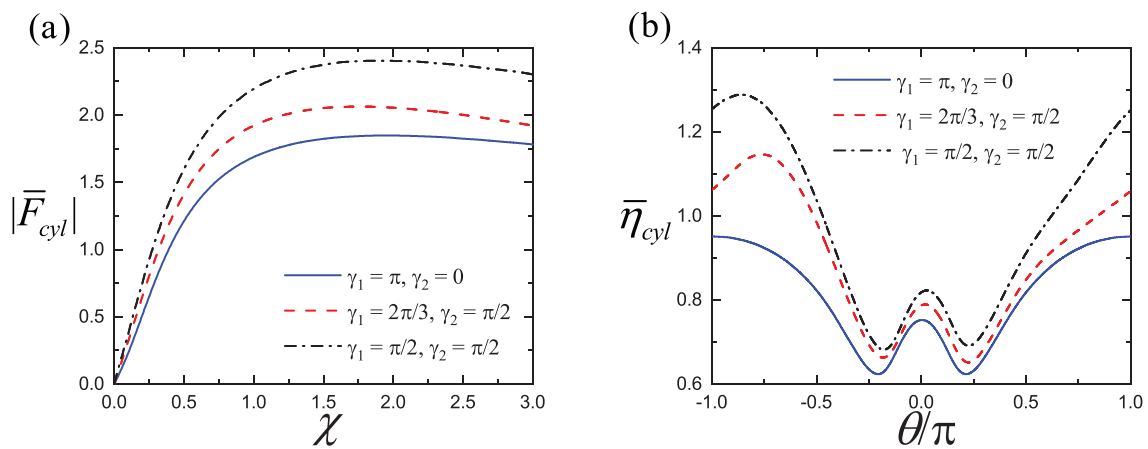


FIG. 19. Variation of the non-dimensional wave force and run-up on the cylinder for three kinds of structure for case 2 with $\alpha_1 = \pi/2, \alpha_2 = \pi, \lambda = 0.5, c/a = 0.5$, and $\beta = 0$: (a) wave force and (b) wave run-up, $\chi = 1$.

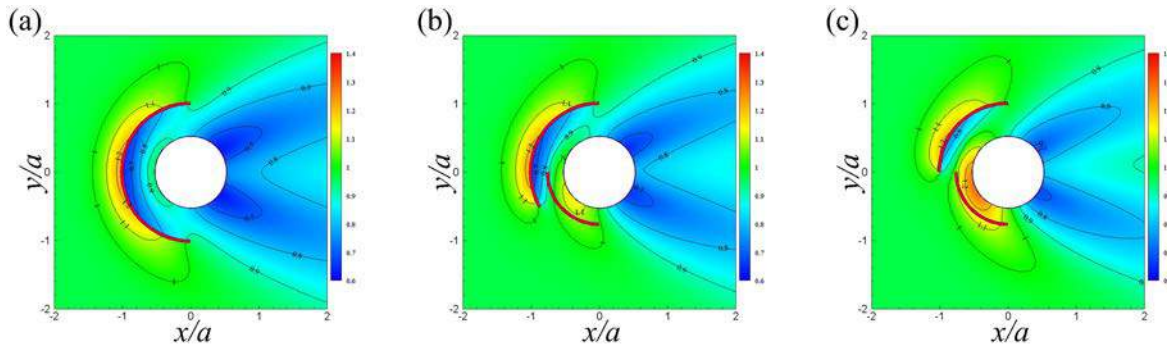


FIG. 20. Distribution of the relative wave height for case 2 with $\beta = 0$, $\chi = 1$, $\alpha_1 = \pi/2$, $\alpha_2 = \pi$, $\lambda = 0.5$, $G_1 = G_2 = 1$, and $c/a = 0.5$: (a) $\gamma_1 = \pi$, $\gamma_2 = 0$, (b) $\gamma_1 = 2\pi/3$, $\gamma_2 = \pi/2$, and (c) $\gamma_1 = \pi/2$, $\gamma_2 = \pi/2$.

height amplitude in the wave region of a cylinder with two uncrossed arcs significantly fluctuates. The force $|\bar{F}_{cyl}|$ and run-up $\bar{\eta}_{cyl}$ on the solid cylinder for case (2) with $\gamma_1 = \gamma_2 = 2\pi/3$, $\alpha_1 = \alpha_2 = 2\pi/3$, $\lambda = 0.5$, and $c/a = 0.5$ are shown in Fig. 19, (a) wave force and (b) wave run-up ($\chi = 1$). For case (2), the trends and amplitudes of the wave force and run-up on the cylinder are similar to those plotted in Fig. 17. The relative wave height change near the combined structure for case (2) is shown in Fig. 20; the calculation conditions are the same as those shown in Fig. 19(b). As shown in Fig. 20(c), when the two arc walls are in uncrossed placement, the wave run-up on the windward side of the interior cylinder is pronounced. The entire protected area in case (1) is larger than that in case (2), resulting in a reduction in wave run-up on the leeward side of the interior cylinder. Overall, the construction of a cylindrical system is not more expensive than building a cylinder with a single-arc wall; moreover, it provides a navigable channel for ships.

V. CONCLUSION

This paper presents an analytical investigation of solitary wave interaction with a combined system having two concentric asymmetric porous arc walls. Based on the present model, several factors influencing the wave loads and run-ups on the interaction cylinder were examined. The correctness of the analytical solution proposed in this paper is verified by comparing its output with the results of existing studies. The main conclusions are summarized as follows:

- (1) The arc structure can only protect a limited area; hence, its performance in terms of wave attenuation may be sensitive to the incident wave heading. Therefore, it is more suitable in unidirectional incident waves such as in the inshore water area.
- (2) The location of arc 2 has a limited effect on protecting the inner cylinder, whereas the degree of permeability of arc walls 1 and 2 has a considerable effect on the wave loads and run-ups on the interior cylinder. Remarkably, the surge phenomenon may occur when $G_2 = 0$ (arc wall 2 is impermeable), possibly risking overtopping.
- (3) The opening angles of the two arc walls are found to considerably affect the wave loads. However, this does not mean that a bigger opening angle is better. After a certain range of opening angles, the solution of reducing the wave load by increasing the opening angle becomes ineffective. In addition, a comparison of two special cases illustrates that a cylinder with double-layered

walls can deal with more complex marine environment than a cylinder with a single-layered wall.

- (4) When two arcs are placed asymmetrically, the protection they provide in reducing wave loads and run-ups becomes less effective; nevertheless, the protection range is extended. As the placement of the two arc walls is crossed, the wave loads and run-ups on the inner cylinder do not significantly increase. Moreover, the gap between the two arcs can be used as a transport corridor, which could be of great importance to engineering applications. In addition, the use of the uncrossed placement of two arc structures in engineering design requires caution due to the relatively inadequate protection it provides.

The case studies presented in this paper are focused on those with $G \in \mathbb{R}^+$. A more general case could be $G \in \mathbb{R}^+ + i\mathbb{R}$ in which the real and imaginary parts represent the resistance and inertia effects of the arc walls, respectively, and this can be studied with the present theoretical model as well. By referring to the results presented here, coastal and ocean structures can be designed more effectively. Because of the specificity of the structure considered in this work, a variety of complex structures for study and discussion may possibly evolve. For example, the single-arc structure, two-arc structure, cylinder with an outer arc wall, and cylinder with two arc walls may be considered. Additionally, the present model can be extended to study solitary wave interaction with a cylinder surrounded by multi-arc walls. The number of elements that has been examined in this work is limited. Nevertheless, the reader can conduct any study of interest based on the formulations presented in this paper.

ACKNOWLEDGMENTS

This work was supported by the National Natural Science Foundation of China (Nos. 52131102 and 51879159), the National Key Research and Development Program of China (No. 2019YFB1704200), and S.Z. gratefully acknowledges the State Key Laboratory of Hydroscience and Engineering (Tsinghua University) for supporting part of this work through the Open Research Fund Program (Grant No. sklhse-2021-E-02).

AUTHOR DECLARATIONS

Conflict of Interest

The authors have no conflicts to disclose.

DATA AVAILABILITY

The data that support the findings of this study are available from the corresponding author upon reasonable request.

REFERENCES

- Basmat, A., "Interaction of a solitary wave with a permeable cylindrical breakwater," *Proc. Appl. Math. Mech.* **1**, 393–394 (2002).
- Chang, K. H., Tsauro, D. H., and Huang, L. H., "Accurate solution to diffraction around a modified V-shaped breakwater," *Coast. Eng.* **68**, 56–66 (2012).
- Cheng, J. S., Miao, G. P., and Wang, J. Q., "Analytical research on wave diffraction on arc-shaped bottom-mounted perforated breakwaters," *China Ocean Eng.* **21**, 417–428 (2007).
- Christensen, E. D., Bingham, H. B., Friis, A. P. S., Larsen, A. K., and Jensen, K. L., "An experimental and numerical study of floating breakwaters," *Coast. Eng.* **137**, 43–58 (2018).
- Chwang, A. T., "A porous-wavemaker theory," *J. Fluid Mech.* **132**, 395–406 (1983).
- Darwiche, M. K. M., Williams, A. N., and Wang, K. H., "Wave interaction with semiporous cylindrical breakwater," *J. Waterw., Port, Coast., Ocean Eng.* **120**, 382–403 (1994).
- Han, X., Dong, S., and Wang, Y., "Interaction between oblique waves and arc-shaped breakwater: Wave action on the breakwater and wave transformation behind it," *Ocean Eng.* **234**, 109252 (2021).
- Isaacson, M. D. S. Q., "Solitary wave diffraction around large cylinder," *J. Waterw., Port, Coast., Ocean Eng.* **109**, 121–127 (1983).
- Li, A. and Liu, Y., "Water wave scattering by a submerged horizontal semi-circular barrier in a two-layer fluid," *Phys. Fluids* **33**, 127102 (2021).
- Liang, H., Zheng, S., Shao, Y., Chua, K. H., Choo, Y. S., and Greaves, D., "Water wave scattering by impermeable and perforated plates," *Phys. Fluids* **33**, 077111 (2021).
- Lin, G. and Liu, J., "Hydrodynamic performance of combined cylinders structure with dual arc-shaped porous outer walls," *Sci. China Phys. Mech. Astron.* **55**, 1963–1977 (2012).
- Liu, J., and Lin, G., "Numerical modelling of wave interaction with a concentric cylindrical system with an arc-shaped porous outer cylinder," *Eur. J. Mech.-B* **37**, 59–71 (2013).
- Liu, J. B., Guo, A. X., Nandasena, N. A. K., Melville, B. W., and Li, H., "Theoretical and experimental investigation on wave interaction with a concentric porous cylinder form of breakwater," *Ocean Eng.* **160**, 156–167 (2018a).
- Liu, H., Zhang, L., Chen, H., Zhang, W., and Liu, M., "Wave diffraction by vertical cylinder with multiple concentric perforated walls," *Ocean Eng.* **166**, 242–252 (2018b).
- Ma, M., Zhang, H., Jeng, D. S., and Wang, C. M., "Analytical solutions of hydroelastic interactions between waves and submerged open-net fish cage modeled as a porous cylindrical thin shell," *Phys. Fluids* **34**, 017104 (2022).
- Miao, Y. and Wang, K. H., "Interaction between a solitary wave and a fixed partially submerged body with two extended porous walls," *J. Eng. Math.* **147**, 04021038 (2021).
- Sankarbabu, K., Sannasiraj, S. A., and Sundar, V., "Interaction of solitary waves with a group of dual porous circular cylinders," in *International Conference on Offshore Mechanics and Arctic Engineering* (ASME, 2008), pp. 307–313.
- Sarkar, A. and Bora, S. N., "Hydrodynamic forces and moments due to interaction of linear water waves with truncated partial-porous cylinders in finite depth," *J. Fluids Struct.* **94**, 102898 (2020).
- Sarkar, A. and Bora, S. N., "Hydrodynamic force and wave run-up due to diffraction of ocean water waves by a surface-piercing bottom-mounted compound partial-porous cylinder," *Fluid Dyn. Res.* **53**, 015508 (2021).
- Song, H. and Tao, L. B., "Short-crested wave interaction with a concentric porous cylindrical structure," *Appl. Ocean Res.* **29**, 199–209 (2007).
- Steiros, K., Kokmanian, K., Bempedelis, N., and Hultmark, M., "The effect of porosity on the drag of cylinders," *J. Fluid Mech.* **901**, R2 (2020).
- Tao, L., Song, H., and Chakrabarti, S., "Wave interaction with a perforated circular breakwater of non-uniform porosity," *J. Eng. Math.* **65**, 257–271 (2009).
- Vijayalakshmi, K., Sundaravadivelu, R., Murali, K., and Neelamani, S., "Hydrodynamics of a concentric twin perforated circular cylinder system," *J. Waterw., Port, Coastal, Ocean Eng.* **134**, 166–177 (2008).
- Wang, K. H. and Ren, X., "Wave interaction with a concentric porous cylinder system," *Ocean Eng.* **21**, 343–360 (1994).
- Weng, Y., Xu, X., and Huang, H., "Interaction of cnoidal waves with an array of vertical concentric porous cylinders," *Appl. Ocean Res.* **58**, 21–36 (2016).
- Williams, A., Li, W., and Wang, K. H., "Water wave interaction with a floating porous cylinder," *Ocean Eng.* **27**, 1–28 (2000).
- Yu, X., "Diffraction of water waves by porous breakwaters," *J. Waterw., Port, Coast., Ocean Eng.* **121**, 275–282 (1995).
- Zamponi, R., Moreau, S., and Schram, C., "Rapid distortion theory of turbulent flow around a porous cylinder," *J. Fluid Mech.* **915**, A27 (2021).
- Zhai, Z., Hu, Q., Ye, W., and Huang, H., "Analytical modelling of solitary wave diffraction from a V-shaped breakwater," *Ocean Eng.* **230**, 109014 (2021a).
- Zhai, Z., Shao, Y., Wang, K., Huang, H., and Li, H., "Semi-analytical solution of cnoidal wave diffraction around a double-layer arc-shaped vertical porous breakwater," *J. Fluids Struct.* **103**, 103261 (2021b).
- Zheng, S., Meylan, M., Greaves, D., and Iglesias, G., "Water-wave interaction with submerged porous elastic disks," *Phys. Fluids* **32**, 047106 (2020a).
- Zheng, S., Porter, R., and Greaves, D., "Wave scattering by an array of metamaterial cylinders," *J. Fluid Mech.* **903**, A50 (2020b).
- Zhong, Z. and Wang, K. H., "Solitary wave interaction with a concentric porous cylinder system," *Ocean Eng.* **33**, 927–949 (2006).